NUREG/CR-5029
SAND87-2384
R7
Printed December 1987

Melt Progression in Severely Damaged Reactor Cores

S. S. Dosanjh

Prepared by
Sandia National Laboratories
Albuquerque, New Mexico 87185 and Livermore, California 94550
for the United States Department of Energy
under Contract DE-AC04-76DP00789

Prepared for
U. S. NUCLEAR REGULATORY COMMISSION

Available from

Superintendent of Documents
U.S. Government Printing Office
Post Office Box 37082
Washington, D.C. 20013-7082

and

National Technical Information Service
Springfield, VA 22161

NUREG/CR-5029
SAND87-2384
R7

MELT PROGRESSION IN SEVERELY DAMAGED REACTOR CORES

S.S. Dosanjh

December 1987

Sandia National Laboratories
Albuquerque, NM 87185
Operated by
Sandia Corporation
for the
U.S. Department of Energy

Prepared for
Division of Reactor System Safety
Office of Nuclear Regulatory Research
U.S. Nuclear Regulatory Commission
Washington, DC 20555
Under Memorandum of Understanding DOE 40-550-75
NRC FIN A1342

ABSTRACT

A model of melt formation and relocation in a two-dimensional core rubble bed is developed in this report. The analysis includes mass conservation equations for the species of interest (UO_2 and ZrO_2); a liquid phase momentum equation (z,r) that incorporates the effects of drag, gravity and capillary forces; and an energy equation that includes internal heat generation by decay heating, convection by the liquid and the solid (as it collapses) as well as conduction and radiation through the bed. An equilibrium UO_2-ZrO_2 phase diagram is prescribed and radiative heat transfer through the bed is incorporated utilizing a temperature-dependent thermal conductivity.

Models developed in this work will be implemented in the MELPROG computer code that is being developed by Sandia and Los Alamos National Laboratories. The modified version of MELPROG will then be used to calculate melt progression, crust growth, pool formation, crust failure and the relocation of debris material into the lower plenum during the Three Mile Island accident and other nuclear reactor accidents.

TABLE OF CONTENTS

LIST OF FIGURES

LIST OF TABLES

NOMENCLATURE

c_p	specific heat at constant pressure [J/kg•K]
d	diameter of the bed [m]
d_p	particle diameter [mm]
D	mass diffusivity [m^2/s]
g	gravitational acceleration [m/s^2]
h	enthalpy [J/kg]
h_f	heat of fusion [J/kg]
J	Leverett function
k	thermal conductivity [W/m•K]
L	bed height [m]
P_c	capillary pressure [N/m^2]
P_g	gas pressure [N/m^2]
P_l	liquid pressure [N/m^2]
Q	decay heat [W/kg of UO_2]
r	radial distance [m]
S	saturation
S_e	effective saturation, $S_e=(S-S_r)/(1-S_r)$
S_r	residual saturation
t	time [s]
T	temperature [K]
u	liquid volumetric flux in the z direction [m/s]
U	velocity at which the solid collapses [m/s]
v	liquid volumetric flux in the r direction [m/s]
Y_{ij}	volume fraction of species j in phase i
z	distance from bottom [m]

Greek

α	volume fraction
α_t	thermal diffusivity [m^2/s]
γ	surface tension [N/m]
ϵ	emissivity
κ	permeability [m^2]
μ	viscosity [Pa•s]
ρ	theoretical density [kg/m^3]
ρ	density [kg/m^3 of total volume]

Subscripts

g	gas
l	liquid
s	solid

1. INTRODUCTION

During severe Light Water Reactor (LWR) accidents involving the loss of coolant, the reactor core can sustain considerable damage. Water present in the reactor vessel at the onset of the accident can be boiled away as energy is released by fission product decay [1]. As temperatures in the reactor core increase, steam from the boiling process oxidizes the zircaloy cladding on the fuel rods, releasing additional energy and forming a ZrO_2 layer on the outside of the cladding [2]. Materials with relatively low melting points, such as silver, liquefy and flow downward as core temperatures increase. When the temperature reaches 2200 K, zirconium melts and starts dissolving UO_2 and ZrO_2 (both of which have melting temperatures above 2800 K) [3]. This U-Zr-O liquid solution flows downward if there is a gap between the cladding and the fuel or if holes form in the ZrO_2 crusts overlying the unoxidized cladding [2]. Zircaloy oxidation ceases if all of the Zr is consumed or if a blockage forms as molten materials flow into lower, colder portions of the core and freeze. During this time, the fuel rods can fragment, converting the core into a large rubble bed [4-7]. If the rods are quenched and subsequently shatter, the particles will be small, with diameters on the order of 1 mm or smaller. A rubble bed can also form in the absence of such an event if the damaged fuel rods collapse; in this case the particles will be approximately the same size as a fuel pellet ($\simeq$1 cm in diameter).

Postaccident analysis of the TMI-2 reactor revealed that the severely damaged core was primarily composed of UO_2 and ZrO_2 particles [4-6]. Of interest to this study is melt progression in such debris beds. Although the energy released by fission product decay falls to less than one-percent of normal operating power one hour after reactor shutdown, temperatures in a dry debris bed can surpass the UO_2 melting point (3100 K) due to the low UO_2 and ZrO_2 thermal conductivities [8,9]. Because dry debris represents a significant risk, the dryout [9-27], quenching and reflooding [28-32] of internally heated particle beds has received considerable attention in the literature. Squarer et al. [10] and Lipinski [11] have presented reviews of recent debris coolability research. Lipinski [12] elucidated much of the physics involved in dryout and developed a steady, one-dimensional model that successfully predicted dryout limits.

Time-dependent models were subsequently developed by E. Gorham-Bergeron [13] and Turland/Moore [14,15]. In-pile D series [16-22] and Degraded Core Coolability [23-24] experiments at Sandia National Laboratories investigated debris dryout in Liquid Metal Fast Breeder Reactors and Light Water Reactors, respectively. Related out-of-pile experiments were conducted by Dhir and Catton [25] and Squarer and Peoples [26].

Relatively little attention has been given to the postdryout meltdown of debris beds that form during LWR accidents. Several Molten Pool [33-37] and Dry Capsule (DC) [38-39] experiments conducted at Sandia National Laboratories investigated incipient debris melting within the context of Liquid Metal Fast Breeder Reactor (LMFBR) accidents. A series of complementary Melt Progression (MP) experiments are being planned at Sandia to study the transition of a dry LWR debris bed to a final molten pool state. The importance of U-Zr-O chemistry will be examined in the MP experiments whereas the earlier LMFBR work stressed UO_2-stainless steel interactions. Larger particles will be used in the MP study (average diameters near 2 mm versus 0.2 mm in the DC experiments) and the temperature gradients will be smaller. Due to large thermal gradients in the DC experiments, evaporation and recondensation was a dominant crust formation process [39].

Natural convection effects in the final molten pool state have been investigated in many LMFBR studies [40-47]. Emara and Kulacki [40], Suo-Anttila and Catton [41], Cheung [42] and Tveitereid [43] modeled natural convection flows in horizontal fluid layers with internal energy generation. Kulacki and Goldstein [44], Baker et al.[45] and Faw et al.[46] present experimental correlations for upward and downward heat partitioning in such fluid layers.

In the present study a two-dimensional model is presented for the postdryout meltdown of a UO_2-ZrO_2 bed to a final state consisting of a molten pool supported by dense solid crusted regions. This model is an extension of earlier work by Kelly [48], who developed a simplified one-dimensional debris meltdown model for use in the MELPROG computer code that is being developed at Sandia and Los Alamos National Laboratories [48,49]. Uncertainties in the MELPROG debris model can affect the manner in which molten material is released into the lower plenum

and fission product release in degraded reactor cores. Conclusions in a recent review [49] of the current MELPROG model follow: a momentum equation should be included in the analysis; the energy balance should be modified so that more realistic phase diagrams can be employed; and a multidimensional model is needed to analyze accidents, such as Three Mile Island, during which radial crust failure is possible. It is anticipated that models developed in the present study will be implemented into MELPROG in the near future.

The equations governing melt relocation are similar to the undersaturated flow equations discussed in Refs. [51-55]. The primary differences are that in the present study source terms are needed in the mass conservation equations to account for phase changes and an energy equation (with an associated phase diagram) must be solved to determine the temperature increase of the bed and the rate of melting and freezing. The model consists of mass conservation equations for the species of interest (UO_2 and ZrO_2); a liquid phase momentum equation that incorporates the effects of drag, gravity and capillary forces; an energy equation that includes internal heat generation by fission product decay, convection by the melt, as well as conduction and radiation through the bed; and an equilibrium UO_2-ZrO_2 phase diagram. Natural convection effects in the molten pool will eventually be included in this model by using the work of Kulacki [44].

A discussion of the model follows. Solutions are presented in Chapter 3 for two particle diameters, 1 mm and 5 mm. Important uncertainties in the model are discussed in Chapter 4. In-pile Melt Progression and out-of-pile MELPROG Validation experiments designed to evaluate the present work and to help guide future work are described.

2. ANALYSIS

Typical characteristics of a UO_2-ZrO_2 core rubble bed similar to the one found in TMI [4] are given in Table I. One hour after reactor shutdown, power generation falls to approximately one percent of peak power [8]. A TMI-2 type plant with an operating power of 2.8×10^3 MW and 93,000 kg of UO_2 in the core [5] has a decay heat Q on the order of 300 W/kg of UO_2. Because it takes several days for the decay heat to decrease significantly below the one hour value [8], it is assumed that Q is constant in the following analysis. A lower limit for the UO_2 volume fraction Y_{s1} is estimated by assuming that all of the roughly 23,000 kg of Zr in a typical core [5] are oxidized, resulting in the formation of 30,000 kg of ZrO_2. Neglecting materials other than UO_2 and ZrO_2 in the core gives a maximum ZrO_2 mass fraction of 0.25. Setting the solid densities of UO_2 and ZrO_2 equal to 10000 and 5700 kg/m^3 [5], respectively, gives a maximum ZrO_2 volume fraction Y_{s2} of 0.36.

TABLE I

Typical initial properties of a core rubble bed.

Quantity of Interest	Typical Value
decay heat, Q [W/kg of UO_2]	300.0
height of bed, L [m]	1.0 [a]
diameter of bed, d [m]	1.0 [a]
particle diameter, d_p [mm]	0.1-10.0 [b]
initial solid volume fraction, α_{si}	0.6 [c]
UO_2 solid volume fraction, Y_{s1}	$\geq$ 0.64
ZrO_2 solid volume fraction, Y_{s2}	$\leq$ 0.36

a. Order of magnitude estimate from Ref. [4].
b. From Ref. [6].
c. Porosity used in bed dryout studies [9].

2.1 Mathematical Formulation

The distance characteristic of changes in the pore structure of the debris bed, d_p, is defined as six times the volume of the solid phase divided by its surface area. The equations governing heat transfer and fluid flow within the bed are amenable to analysis for a particular range of d_p. When d_p is on the order of the mean free path of the gas molecules, λ, corresponding to the Knudsen limit, the diffusion models employed in this study must be modified. On the other hand, when d_p is large, of the same order as x_c, the distance characteristic of changes in temperature and species concentrations, the particles must be considered individually. The following analysis is restricted to debris beds in which d_p satisfies $\lambda << d_p << x_c$.

2.1.1 Conservation of Mass

Species diffusion is neglected in the following analysis. Typical mass diffusivities for liquids near their melting points are on the order of 10^{-9} m^2/s [56]. For time scales on the order of 10^3 s, the distance characteristic of diffusion, $[Dt]^{1/2}$, is approximately 10^{-3} m. That is, liquid phase diffusion is only important over length scales comparable to the average particle diameter. Balancing the mass stored in a differential control volume, convection by the liquid and the solid (as it collapses) and production (or depletion) by melting gives for species j (j=1 and j=2 correspond to UO_2 and ZrO_2, respectively)

$$\frac{\partial}{\partial t}\left[Y_{1j}\rho_{1j}\alpha_1\right] = -\frac{\partial}{\partial z}\left[Y_{1j}\rho_{1j}u\right] - \frac{1}{r}\frac{\partial}{\partial r}\left[rY_{1j}\rho_{1j}v\right]$$

$$-\frac{\partial}{\partial z}\left[Y_{sj}\rho_{sj}\alpha_s U\right] - \frac{\partial}{\partial t}\left[Y_{sj}\rho_{sj}\alpha_s\right] \quad , \qquad (1)$$

where the subscripts 1 and s refer to liquid and solid, respectively. The quantities α_s and α_l are solid and liquid volume fractions, respectively, $\underline{u}=(u,v)$ is the liquid volumetric flux, U is the velocity at which the solid collapses downward, ρ_{ij} is the theoretical density of species j in phase i and Y_{ij} is the portion of phase i that is occupied by species j. The Y_{ij}'s are related to each other by $Y_{11}+Y_{12}=1$ and $Y_{s1}+Y_{s2}=1$.

2.1.2 Liquid Phase Velocities

Assuming that the liquids are miscible, Darcy's Law gives for the momentum equations,

$$\rho_l \frac{\partial u}{\partial t} + \frac{\mu}{\kappa_l} u = - \frac{\partial}{\partial z} P_l - g\rho_l \quad , \tag{2a}$$

and

$$\rho_l \frac{\partial v}{\partial t} + \frac{\mu}{\kappa_l} v = - \frac{\partial}{\partial r} P_l \quad , \tag{2b}$$

where μ is the dynamic viscosity of the liquid, g is the gravitational acceleration and κ_l is the relative permeability. Equations (2a,2b) take into account viscous drag, which is assumed to vary linearly with velocity, gravity and motion due to changes in pressure. Capillary forces enter Eqs.(2a,2b) through the terms involving the liquid pressure, P_l. The capillary pressure is defined as the difference between P_l and the gas pressure, P_g (that is, $P_c=P_g-P_l$) [51-55]. Taking the gas flow to be isobaric gives $\nabla P_l=-\nabla P_c$. From Eqs.(2a,2b) it is therefore evident that capillary forces move liquid into regions of high P_c.

Leverett [55] derived the following relation for P_c using dimensional analysis,

$$P_c = J\gamma\left[\frac{1-\alpha_s}{\kappa}\right]^{1/2} \quad , \tag{3}$$

where γ is the surface tension, κ is the permeability and J is the Leverett function. He further noted that J is only a function of the saturation

$$S \equiv \frac{\alpha_l}{\alpha_l+\alpha_g} \quad , \tag{4}$$

and the residual saturation S_r (which is defined as the threshold value of S below which bulk liquid motion ceases). Physically, S

represents the fraction of the porosity that is occupied by liquid. Bird et al. [57] derive a relation for κ by modelling the porous solid as a bundle of capillary tubes,

$$\kappa = \frac{d_p^2 \ (1-\alpha_s)^3}{150 \ \alpha_s^2} \quad , \tag{5}$$

where the factor of 150 is determined empirically. Combining Eq.(3,5) gives

$$P_c = J\gamma \ \frac{\sqrt{150} \ \alpha_s}{d_p(1-\alpha_s)} \quad , \tag{6}$$

Note that P_c decreases as the particle diameter d_p, increases. For $\gamma \approx 0.5$ N/m, capillary forces are only important when d_p is on the order of 1 mm (or smaller) [50]. Increasing α_s increases P_c and consequently, capillary forces tend to move liquid into regions of higher solid fraction (lower porosity).

Empirical correlations are needed for J, the relative permeability κ_l, and the residual saturation S_r. Hofmann and Barleon [58] give for J

$$J = a \ (S_e + b)^{-c} \quad , \tag{7}$$

where S_e $[\equiv (S-S_r)/(1-S_r)]$ is an effective saturation, a=0.38, b=0.014 and c=0.27. Equation (7) agrees with the results of Reed et al [23] except near $S_e=0$. The primary advantage of Eq.(7) is the absence of a singularity at $S_e=0$. Note that J and P_c reach their maximum value in regions of low saturation. Therefore, capillary forces tend to move liquid into regions of low saturation [51-55].

In fully saturated flow ($S=S_e=1$), κ_l equals the permeability, κ, while in undersaturated flow, only a fraction of the solid is wetted and κ_l is proportional to κ (with the proportionality being a function of S). Reed et al. [23] give for κ_l

$$\kappa_l = \begin{cases} \kappa S_e^3 & , \text{ for } S > S_r \\ 0 & , \text{ for } S \leq S_r \end{cases} \qquad (8)$$

where $S_e=(S-S_r)/(1-S_r)$. As discussed earlier, liquid does not begin to flow until the saturation reaches a threshold value, S_r. For $S \leq S_r$, $\kappa_l=0$ and Eq.(2) requires that q=0. When S is less than S_r, the liquid consists of unconnected pendular rings. Liquid starts to flow when S is increased to the point that these rings touch and coalesce [55].

Brown et al. [59] give for the residual saturation S_r,

$$S_r = \frac{1}{86.3} \left[\frac{\gamma}{\kappa \rho_l g}\right]^{0.263} \qquad (9)$$

Thus, S_r varies with the ratio of surface tension to gravity. The dependence of S_r on the porous matrix is contained in the permeability κ. Increasing the particle diameter or the porosity raises κ and leads to lower values of S_r. For packed beds consisting of small, tightly packed particles, the saturation must be increased to a high value before bulk liquid motion is observed.

2.1.3 Solid Collapse

As solid melts in the center of the bed and flows outward under the action of gravity and capillary forces, the porosity in the melt zone increases. In-pile experiments have indicated that the melt zone can be self-supporting at high porosities (up to 0.7) [33-37]. In this study it is assumed that debris starts collapsing when the solid fraction decreases to a critical value $\alpha_{s,min}$ and that $\alpha_s=\alpha_{s,min}$ in regions into which solid is settling. Experiments are needed to determine $\alpha_{s,min}$ as a function of particle diameter and initial porosity. Uncertainties in $\alpha_{s,min}$ will affect the configuration of the melt zone and the growth of the molten pool. In the calculations presented in Chapter 3 $\alpha_{s,min}$ is set equal to 0.3 and most of the discussion is focused on pre-collapse phenomenon.

2.1.4 Conservation of Energy

Assuming that all the materials present are in local thermal equilibrium, only one temperature field needs to be determined. Radiation heat transfer in the packed bed is incorporated utilizing a diffusion model with a temperature dependent conductivity. Balancing the energy stored in the solid and the liquid, convection by the liquid and the solid (as it collapses), diffusion and internal heat generation,

$$\frac{\partial}{\partial t}\sum_j \left[\alpha_s Y_{sj}\rho_{sj}h_{sj} + \alpha_l Y_{lj}\rho_{lj}h_{lj}\right] = -\frac{\partial}{\partial z}\left[U\sum_j Y_{sj}\alpha_s\rho_{sj}h_{sj}\right]$$

$$-\frac{\partial}{\partial z}\left[u\sum_j Y_{lj}\rho_{lj}h_{lj}\right] - \frac{1}{r}\frac{\partial}{\partial r}\left[rv\sum_j Y_{lj}\rho_{lj}h_{lj}\right]$$

$$+\frac{\partial}{\partial z}k_{eff}\frac{\partial T}{\partial z} + \frac{1}{r}\frac{\partial}{\partial r}rk_{eff}\frac{\partial T}{\partial r}$$

$$+\left[\alpha_s\rho_{s1}Y_{s1} + \alpha_l\rho_{l1}Y_{l1}\right]Q\ , \qquad (10)$$

where h_{ij} is the enthalpy of species j in phase i, Q is the decay heat expressed as energy release per mass of UO_2 and k_{eff} is an effective thermal conductivity which accounts for both conductive and radiative heat transfer in the porous solid. Note that energy stored in the gas phase is neglected in Eq.(10). This is a reasonable approximation because the densities of materials of interest are very large (on the order of 10^4 kg/m^3) compared with the gas density.

Radiation heat transfer in the packed bed is incorporated using a modified gas conductivity, $k_g^* = k_g + k_{rad}$ [60,61]. That is, it is assumed that gas conduction and radiation act in parallel. Several researchers [60-64] have proposed that $k_{rad} = 4\epsilon\sigma d_p T^3$, where ϵ is the emissivity of the solid and σ is the Stefan-Boltzmann constant. Empirical correlations for k_{eff} in solid-gas systems are available in the literature [60,61,64]. However, in the current problem, three phases (solid, liquid and gas) are present. In calculating k_{eff}, the solid and the liquid are treated as a single component with a volume averaged thermal conductivity,

$$k_\sigma = \frac{1}{\alpha_s + \alpha_l}\left[\alpha_s \sum_j Y_{sj}k_{sj} + \alpha_l \sum_j Y_{lj}k_{lj}\right] \quad , \tag{11}$$

where k_{ij} is the conductivity of species j in phase i. For a single phase i, k_σ depends only on Y_{ij} and k_{ij}. That is, $k_\sigma = Y_{s1}k_{s1} + Y_{s2}k_{s2}$ for $\alpha_l = 0$ (solid only) and $k_\sigma = Y_{l1}k_{l1} + Y_{l2}k_{l2}$ for $\alpha_s = 0$ (liquid only). The following correlation is used to calculate k_{eff} [60,64],

$$k_{eff} = \psi\, k_g^* + \frac{1-\psi}{k_\sigma\omega + k_g^*(1-\omega)}\, k_\sigma k_g^* \quad , \tag{12}$$

where

$$\omega = 0.3\, \alpha_g^{1.6}(k_\sigma/k_g^*)^{-0.044} \quad , \tag{13}$$

$$\psi = \frac{\alpha_g - \omega}{1-\omega} \quad , \tag{14}$$

and α_g is the volume fraction occupied by gas. Note that as $\alpha_g \to 0$, $\omega \to 0$, $\psi \to 0$ and consequently, $k_{eff} \to k_\sigma$. As $\alpha_g \to 1$, $\psi \to 1$, giving $k_{eff} \to k_g^*$.

2.1.5 Closure

In order to complete Eqs. (1-14) a phase diagram, initial conditions, boundary conditions and properties must be specified. Shown in Fig.1 is an equilibrium phase diagram for a homogeneous UO_2-ZrO_2 mixture. Figure 1 was constructed from the solidus and liquidus temperatures (T_s and T_l, respectively) given in Ref. [65]. Experiments needed to check the validity of the equilibrium assumption are discussed in Chapter 4. A discussion of the effect of diffusion at the particulate level is given by Dosanjh [50].

An initial uniform temperature T_i is prescribed. Boundaries continue to radiate to environments at this temperature as the bed temperature increases. The bed is assumed to have an initial porosity of 0.4 and the composition of the bed is taken to be uniform over distances characteristic of changes in T, S and α.

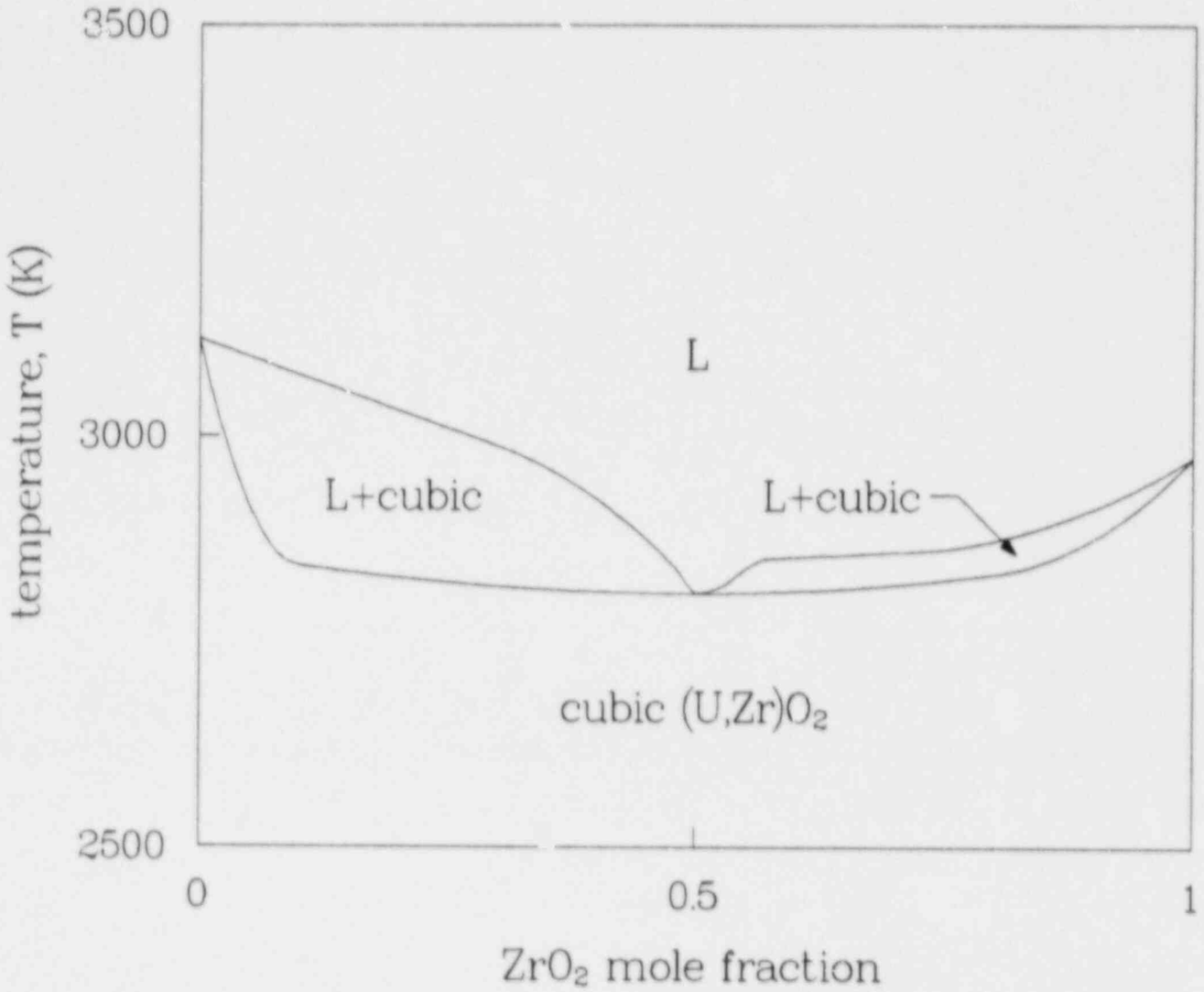

FIG. 1: Phase diagram for UO_2–ZrO_2.

Typical values of densities ρ_{ij}, specific heats c_{pij}, heats of fusion h_{fj}, thermal conductivities k_{ij}, viscosities μ_j and surface tensions γ_j for UO_2 and ZrO_2 are given in Table II. Initial measurements of the liquid UO_2 thermal conductivity ranged from 2.0 W/(mK) to 11.0 W/(mK) [66,67]. Upon subsequent analysis of these experiments, Fink and Leibowitz [71] suggested a value of 5.5 W/(mK). The gas is taken to be argon, for which $k_g = 2.986 \times 10^{-4} T^{0.7224}$, where k_g is measured in W/m•K and T is in Kelvins [3]. The viscosity of the melt is calculated by volume averaging. For simplicity, properties are assumed to remain constant in the calculations presented here.

TABLE II

Typical UO_2 and ZrO_2 properties given in Refs. [3,65-72].

Property	UO_2 (j=1)	ZrO_2 (j=2)
theoretical solid density, ρ_{sj} [kg/m^3]	9,650	5,700
liquid density, ρ_{lj} [kg/m^3]	8,700	5,700
solid specific heat, c_{psj} [J/kg•K]	630	700
liquid specific heat, c_{plj} [J/kg•K]	490	815
solid thermal conductivity, k_{sj} [W/m•K]	3.0	2.0
liquid thermal conductivity, k_{lj} [W/m•K]	5.5	2.7
heat of fusion, h_{fj} [J/kg]	274,000	706,000
viscosity, μ_j [Pa•s]	0.0058	0.0035
surface tension, γ_j [N/m]	0.45	0.45

2.2 Order of Magnitude Analysis

Consider a debris bed with an initial temperature profile, $T_i(z,r)=T(z,r,0)$. If the distance characteristic of changes in T_i is on the order of L, the height of the bed, conduction and radiation in the bed become important over the entire domain at time $t=L^2/\alpha_t$, where α_t is an average solid thermal diffusivity. Using the UO_2 properties in Table II, setting $\epsilon=0.4$ and evaluating k_{eff} at 2000 K, gives $\alpha_t \simeq k_{eff}/[(1-\epsilon)\rho_s c_{ps}] \simeq 10^{-6}$ m^2/s. Rubble beds with heights on the order of 1 m heat up adiabatically until time $L^2/\alpha_t \simeq 10^6$ s. For the times of interest, T(z,r,t) is highly dependent on initial conditions and

conduction and radiation are only important within boundary layers of thickness $\delta \simeq [\alpha_t t]^{1/2}$. In the region $\delta << x << L-\delta$,

$$T(z,r,t) - T(x,r,0) = \frac{Y_{s1}\rho_{s1} Q\, t}{\sum_{j=1}^{2} Y_{sj}\rho_{sj} c_{psj}} \quad , \tag{15}$$

which is valid until melt forms. Setting Q = 300 W/kg of UO_2, Y_{s1} = 0.64 and utilizing the properties in Table II gives a 0.35 K/s as an approximate lower bound for the heating rate. For beds composed of only UO_2 particles (Y_{s1}=1), Eq.(15) gives a heating rate of 0.5 K/s. Therefore, it takes between 2000 s and 2860 s for the temperature of the bed to increase by 1000 K.

2.3 Solution Algorithm

Equations (1.2,10) along with auxiliary relations (3-9,11-14) are solved using an explicit finite difference scheme. Solution of these equations is somewhat complicated by the fact that time derivatives appearing in Eqs.(1,10) involve products of the primitive variables, T, α_s, α_1, Y_{s1}, Y_{s2}, Y_{11} and Y_{12}. Given the values of all variables at a time step n, the solution algorithm is as follows. The velocity field is calculated at cell boundaries utilizing Eq.(2) and information at step n. Next, the bulk densities (which are based on total volume) of UO_2 and ZrO_2,

$$\tilde{\rho}_{UO_2} = \alpha_s Y_{s1}\rho_{s1} + \alpha_1 Y_{11}\rho_{11} \quad , \tag{16}$$

and

$$\tilde{\rho}_{ZrO_2} = \alpha_s Y_{s2}\rho_{s2} + \alpha_1 Y_{12}\rho_{12} \quad , \tag{17}$$

respectively, and the enthalpy function,

$$H = \sum_j \left[\alpha_s Y_{sj}\rho_{sj} h_{sj} + \alpha_1 Y_{1j}\rho_{1j} h_{1j} \right] \quad , \tag{18}$$

are calculated at time step n+1 at each calculation node from Eqs.(1,10). When only one phase is present, solution of

Eqs.(1,10) is straightforward. In two phase regions, the phase diagram provides additional relations of the form

$$\frac{Y_{s2}\rho_{s2}/M_2}{\sum_{j=1}^{2} Y_{sj}\rho_{sj}/M_j} = f(T) \qquad (19)$$

and

$$\frac{Y_{12}\rho_{12}/M_2}{\sum_{j=1}^{2} Y_{1j}\rho_{1j}/M_j} = g(T) \qquad (20)$$

where M_j is the molecular weight of species j and f and g are specified functions of temperature. Terms on the left hand sides of Eqs.(19,20) represent mole fractions of ZrO_2 in the solid and liquid phases, respectively. Equations (16-20) along with the relations, $Y_{s2}=1-Y_{s1}$ and $Y_{12}=1-Y_{11}$, are then solved for the primitive variables, T, α_s, α_1, Y_{s1}, Y_{s2}, Y_{11} and Y_{12}.

3. RESULTS AND DISCUSSION

Solutions are presented in the following sections for a 0.5 m high UO_2-ZrO_2 porous bed with a diameter of 0.5 m, an average particle diameter of 1 mm, an initial uniform porosity of 0.4 and a ZrO_2 to UO_2 mass ratio of 0.1. The bed is initially at a uniform temperature of 1500 K and the boundaries continue to radiate to an environment at 1500 K as the temperature of the bed increases due to decay heating. It is assumed in these calculations that the solid begins collapsing when α_s=0.3. The effect of varying the particle diameter will be discussed in section 3.2.

3.1 Base Case

Temperature contours in the bed at t=3200 s are shown in Fig. 2. Because of the low thermal conductivities involved, the temperature in the bed is fairly uniform except in narrow thermal boundary layers. For a ZrO_2 to UO_2 mass ratio of 0.1 (which corresponds to a ZrO_2 mole fraction of 0.18), Fig.1 gives a solidus temperature of 2830 K. Therefore, the 2800 K contour approximately encloses the melt zone. A plot of the solid fraction α_s at this time is shown in Fig. 3. Note that α_s has decreased in the center of the bed (there is a corresponding increase in α_l). No liquid motion is evident because the saturation is below the critical residual saturation S_r. That is, liquid is held in place by surface tension effects.

Liquid motion is evident at t=3400 s (see Fig.4). Melt flowing downward and radially outward has refrozen, forming a crust as evidenced by the appearance of the cross hashed region. Radial relocation is driven by capillary forces, which tend to move liquid into regions of higher solid fraction. Downward relocation is due to both gravity and capillary forces. A crust has not formed above the melt zone at this time because gravity opposes upward relocation. As shown by the contours in Fig. 5, temperatures in regions adjacent to the melt zone increase as liquid freezes, giving up its heat of fusion.

Because the beds of interest are rich in UO_2, the ZrO_2 mole fraction is initially larger in the liquid than in the solid (see Fig. 1). As liquid relocates the local ZrO_2 mass fraction

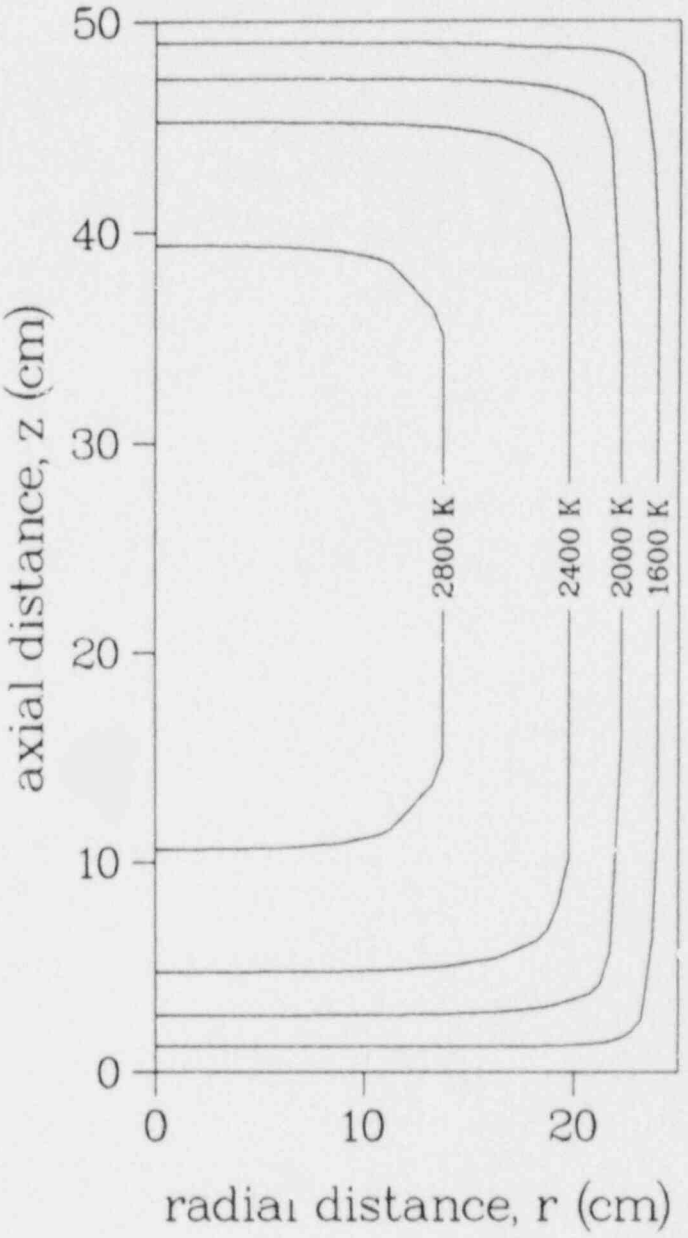

FIG. 2: Temperature contours in rubble bed at t=3200 s for the base case. Contours are shown every 400 K.

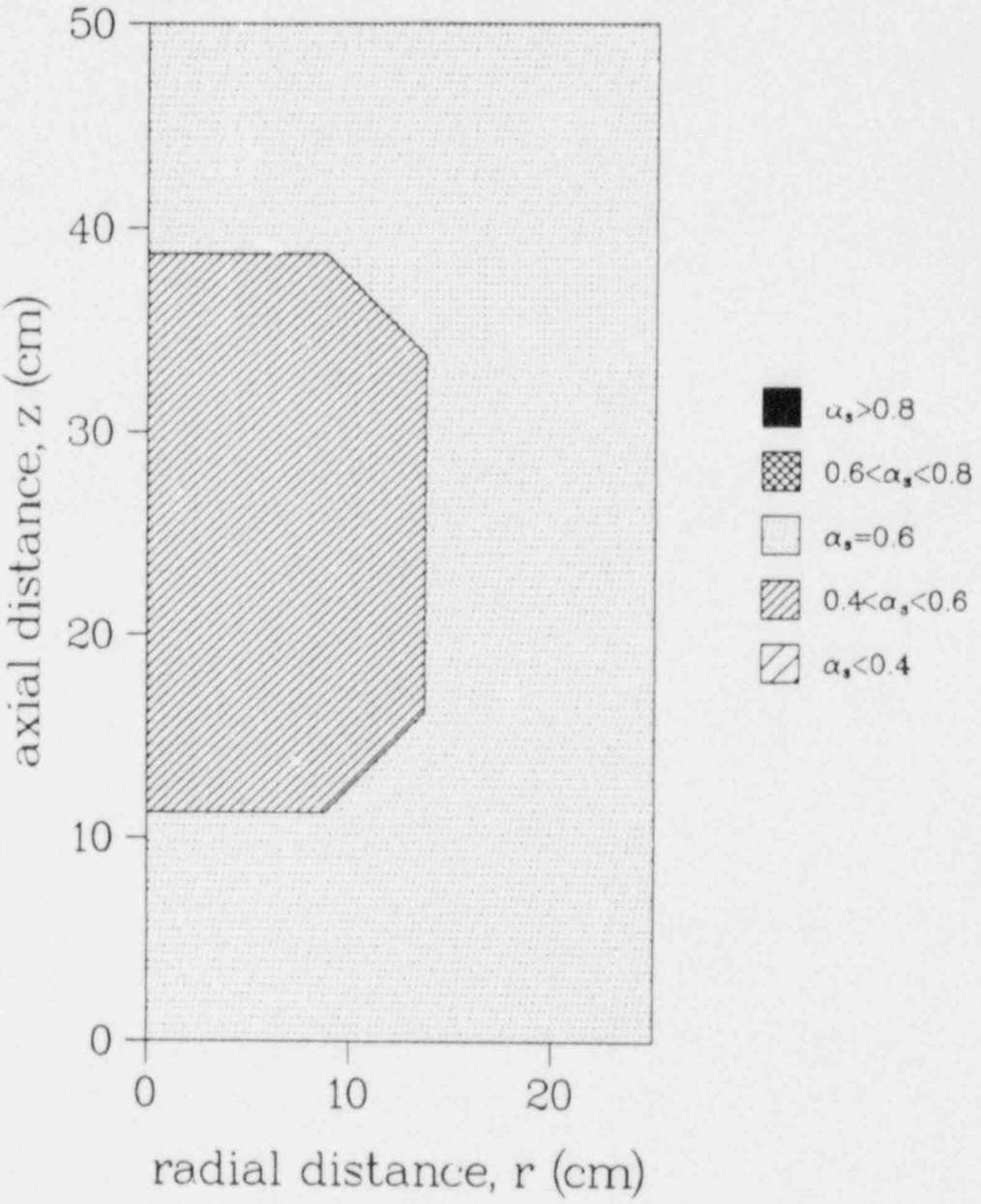

FIG. 3: Solid volume fraction α_s in rubble bed at t=3200 s for the base case. The rubble has an initial uniform solid volume fraction of 0.6.

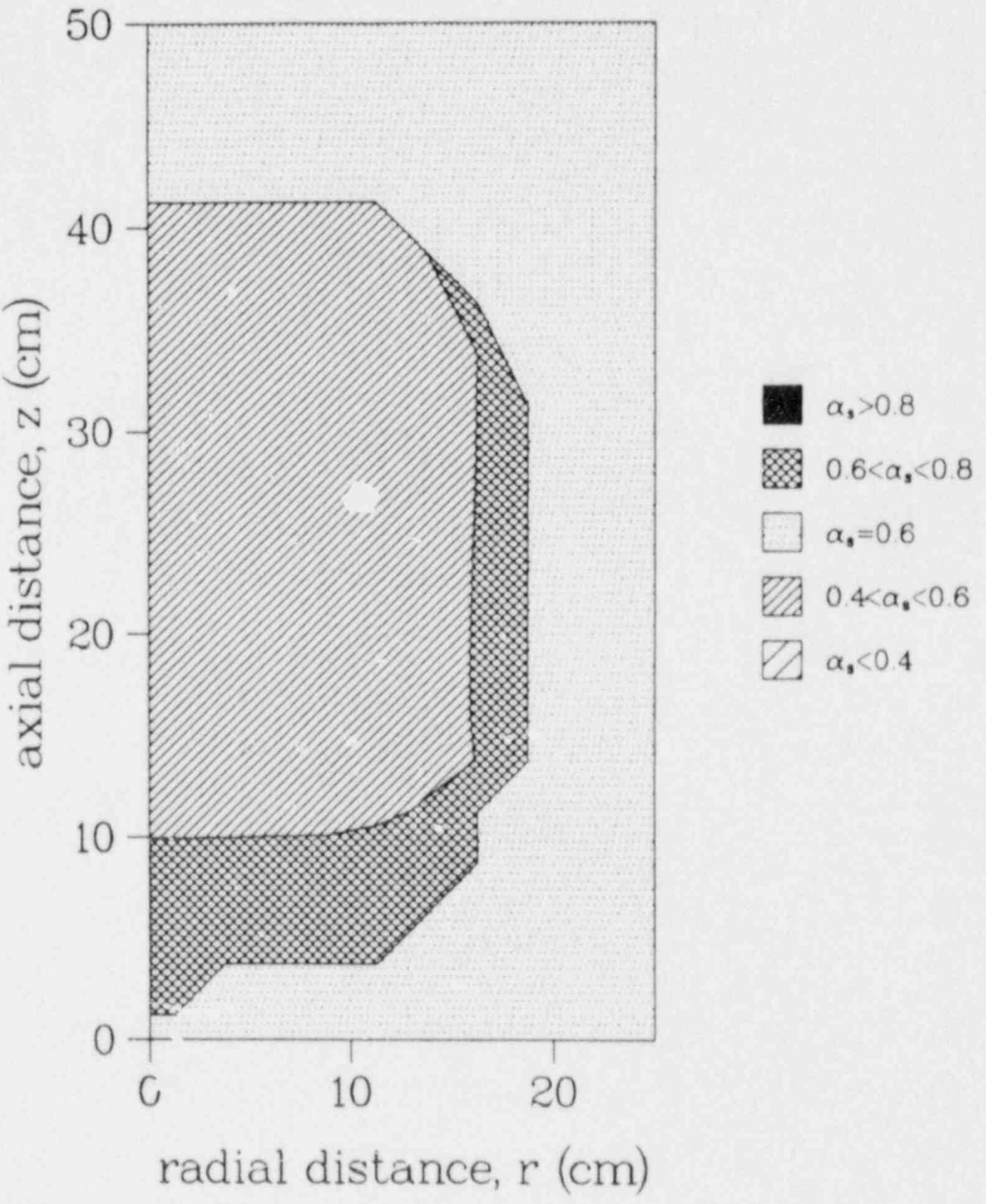

FIG. 4: Solid volume fraction α_s in rubble bed at t=3400 s for the base case. The rubble has an initial uniform solid volume fraction of 0.6.

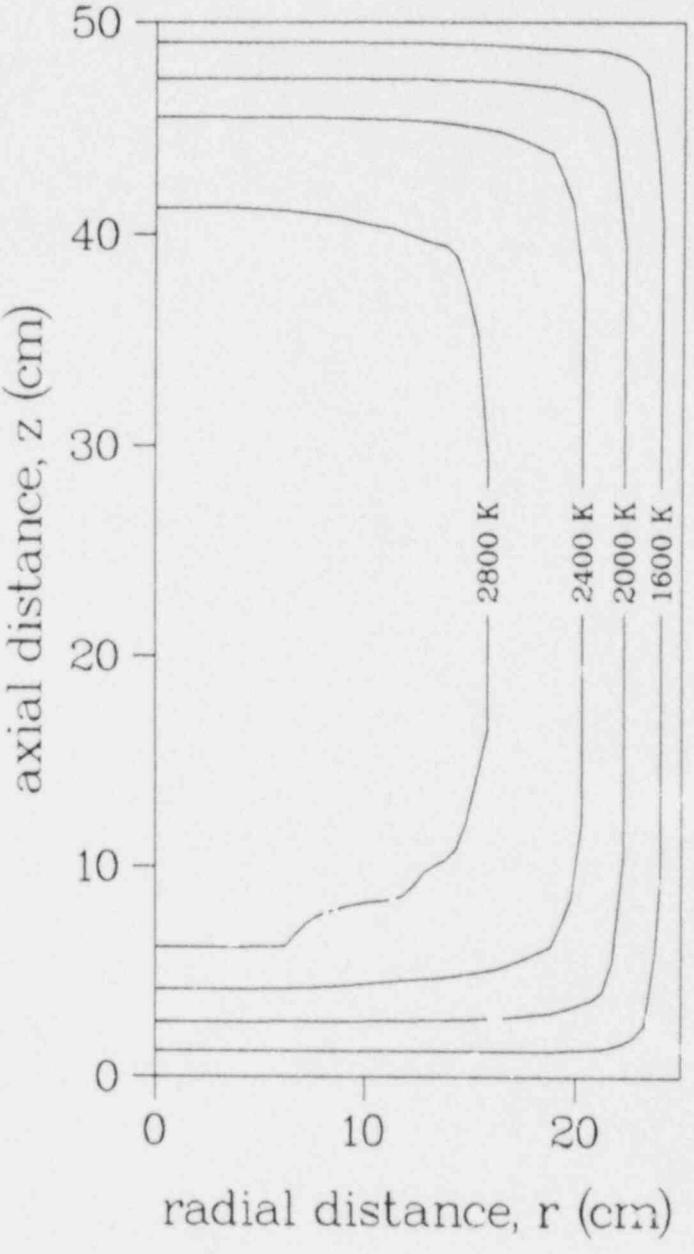

FIG. 5: Temperature contours in rubble bed at t=3400 s for the base case. Contours are shown every 400 K.

changes. A normalized UO_2 to ZrO_2 mass ratio η is defined such that η=1 initially. In a bed with an initial ZrO_2 mole fraction of 0.5, the solidus and liquidus temperatures both equal 2810 K and consequently, η remains uniform as melt forms and relocates. Contours of η at 3400 s and 3600 s for the base case are shown in Figs. 6 and 7, respectively. Note that ZrO_2 is depleted in the center of the bed and accumulates in the crust regions. At t=3600 s, η varies from 0.5 in the center to 2.0 in the crust and the ZrO_2 mole fraction changes from 0.1 to 0.3.

A blockage has formed below the melt zone before 3600 s elapse (see Fig. 8). Up to this time most of the melt has flowed downward under the action of gravity. As the solid fraction in the center of the bed continues to decrease, gradients of α_s and P_c (which is related to α_s by Eq.6) increase. That is, the driving force for capillary forces increases with time. As evidenced by Fig. 9, the solid fraction in the center of the bed is below 0.4 at t=3800 s and a crust has begun to form above the melt zone.

The low solid fraction region (α_s<0.4) in Fig. 9 continues to grow during the next 400 s (see Figs. 10 and 11). Liquid volume fractions at t=4200 s are shown in Fig. 12. A two phase (liquid-solid) molten pool forms above the blockage as liquid accumulates. A small amount of liquid (α_l<0.1) is suspended in the melt zone above this region by surface tension effects. Note that the liquid level increases towards the edges of the pool. This wicking is due to the variation of capillary rise x_c with solid fraction. An approximate relation for x_c can be obtained by balancing gravity and capillary forces in Eq.(2a), giving

$$x_c \simeq \frac{\sqrt{150}\, a\gamma\alpha_s}{d_p \rho_g (1-\alpha_s)} \qquad (21)$$

In the region to the left of the blockage in Fig. 10, α_s increases with r. Consequently, x_c increases near the edges of the pool. In the next section it will be shown that this effect is negligible for 5 mm diameter particles. The gas volume fraction, $\alpha_g=1-\alpha_s-\alpha_l$, at 4200 s is plotted in Fig.13. In the molten pool, the gas fraction is zero and the flow is fully

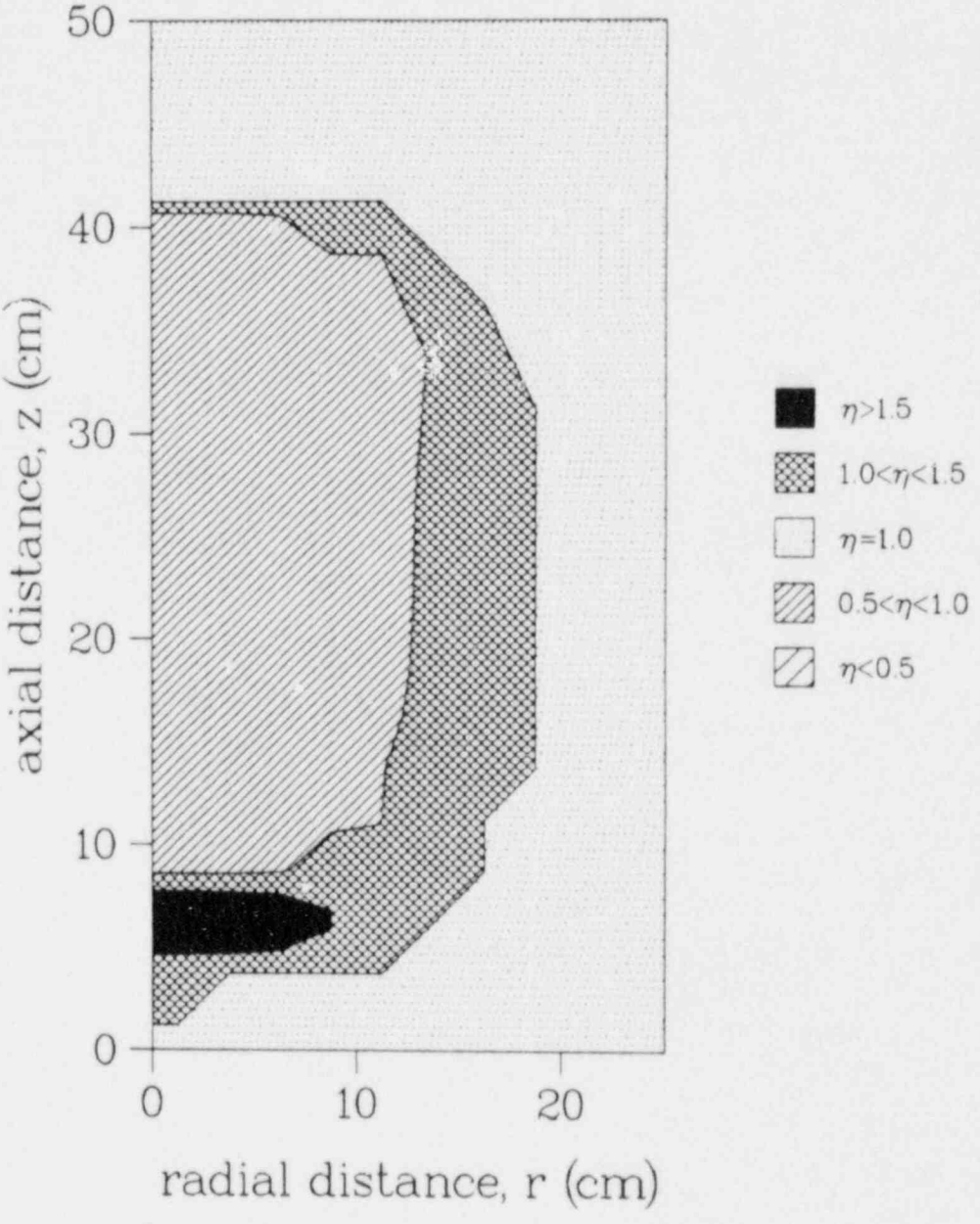

FIG. 6: Normalized ZrO_2 to UO_2 mass ratio η at t=3400 s for the base case.

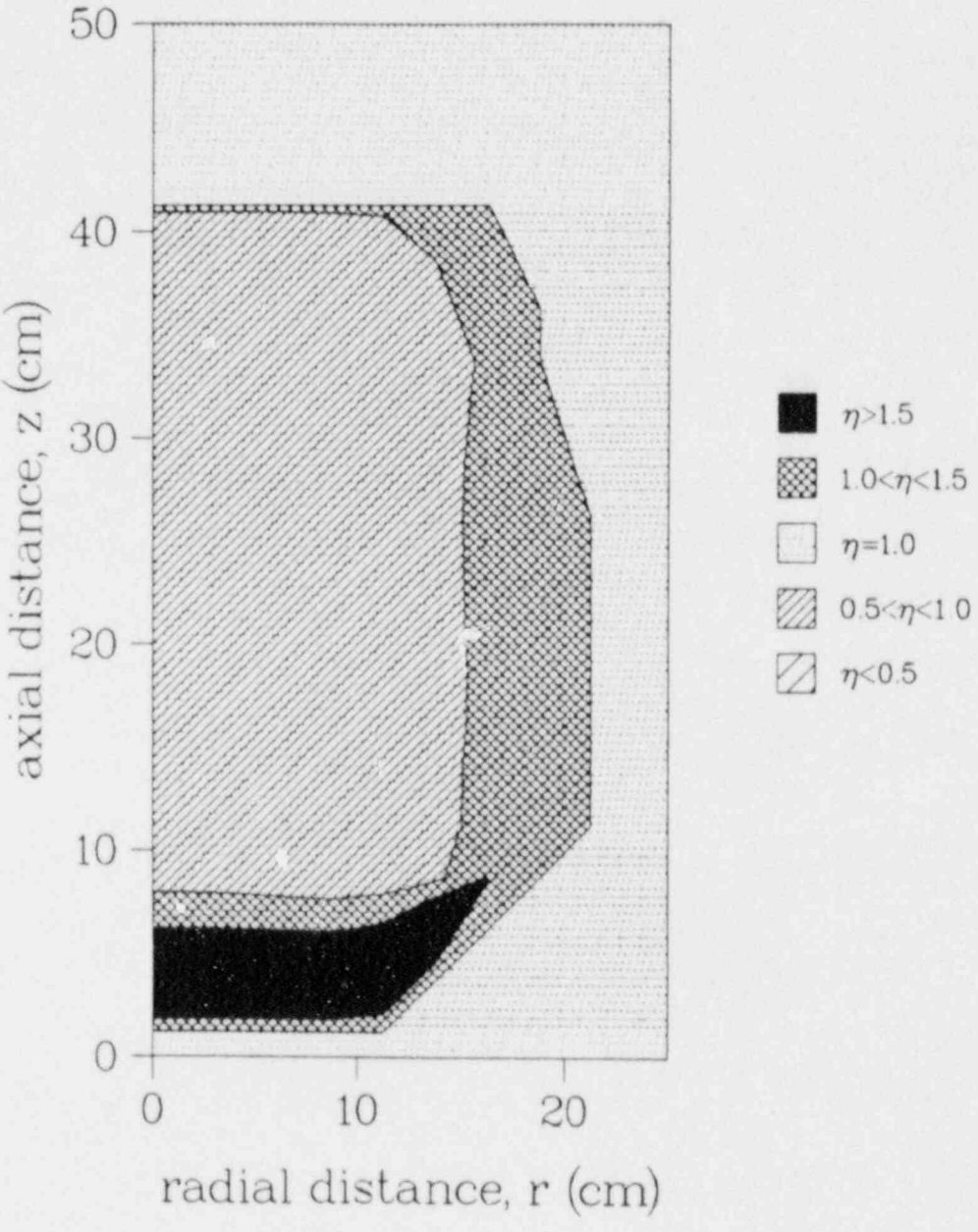

FIG. 7: Normalized ZrO_2 to UO_2 mass ratio η at t=3600 s for the base case.

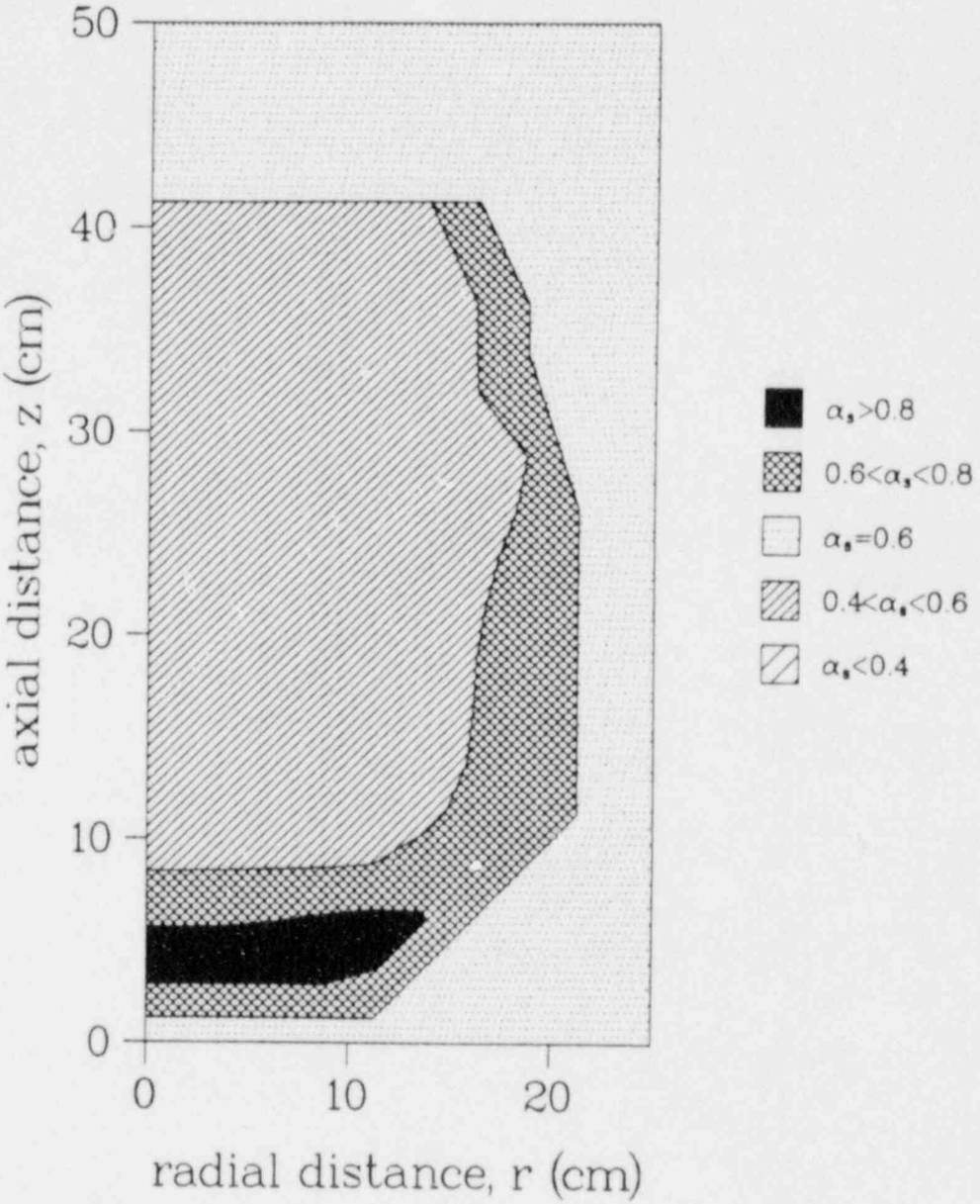

FIG. 8: Solid volume fraction α_s in rubble bed at t=3600 s for the base case. The rubble has an initial uniform solid volume fraction of 0.6.

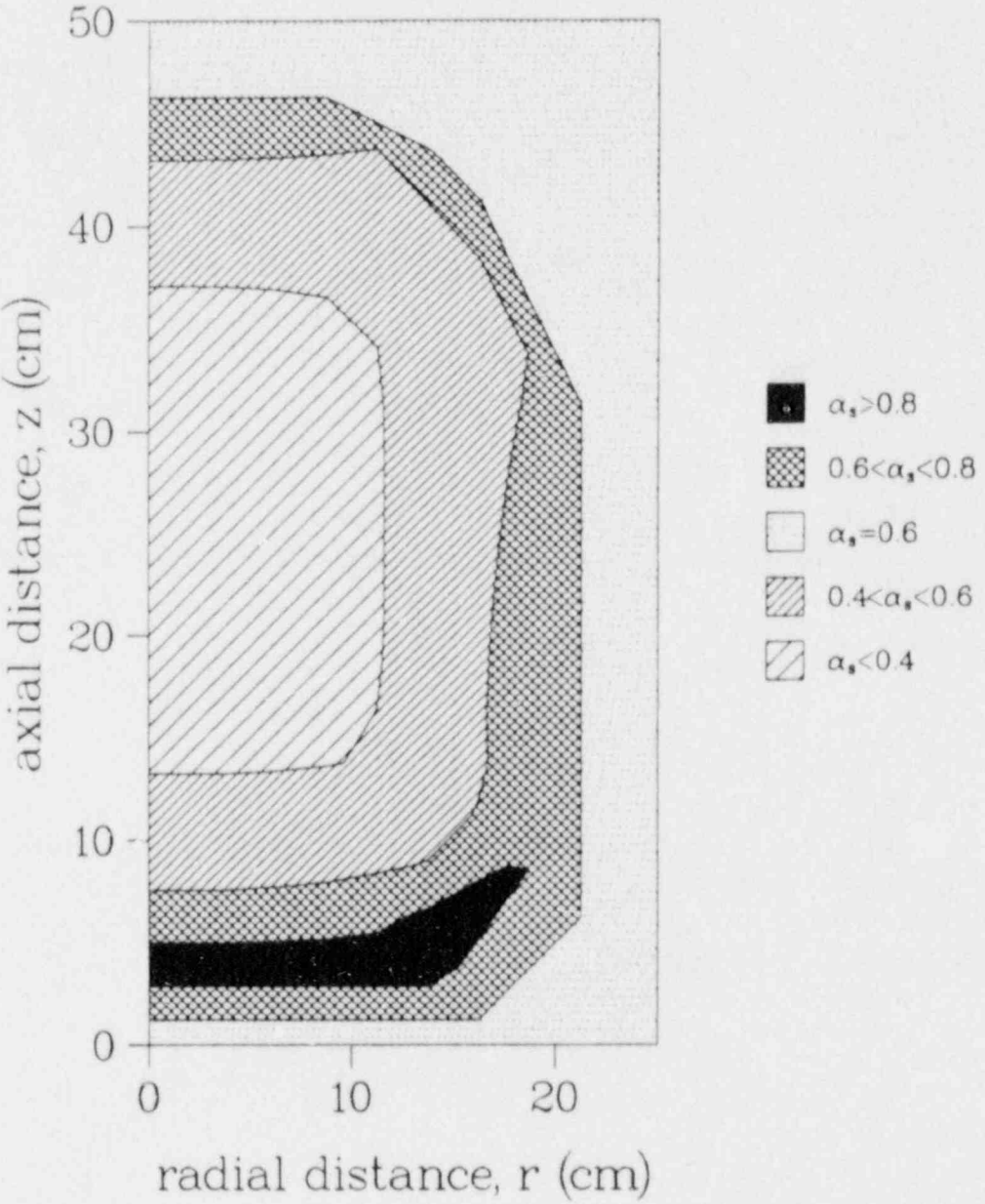

FIG. 9 Solid volume fraction α_s in rubble bed at t=3800 s for the base case. The rubble has an initial uniform solid volume fraction of 0.6.

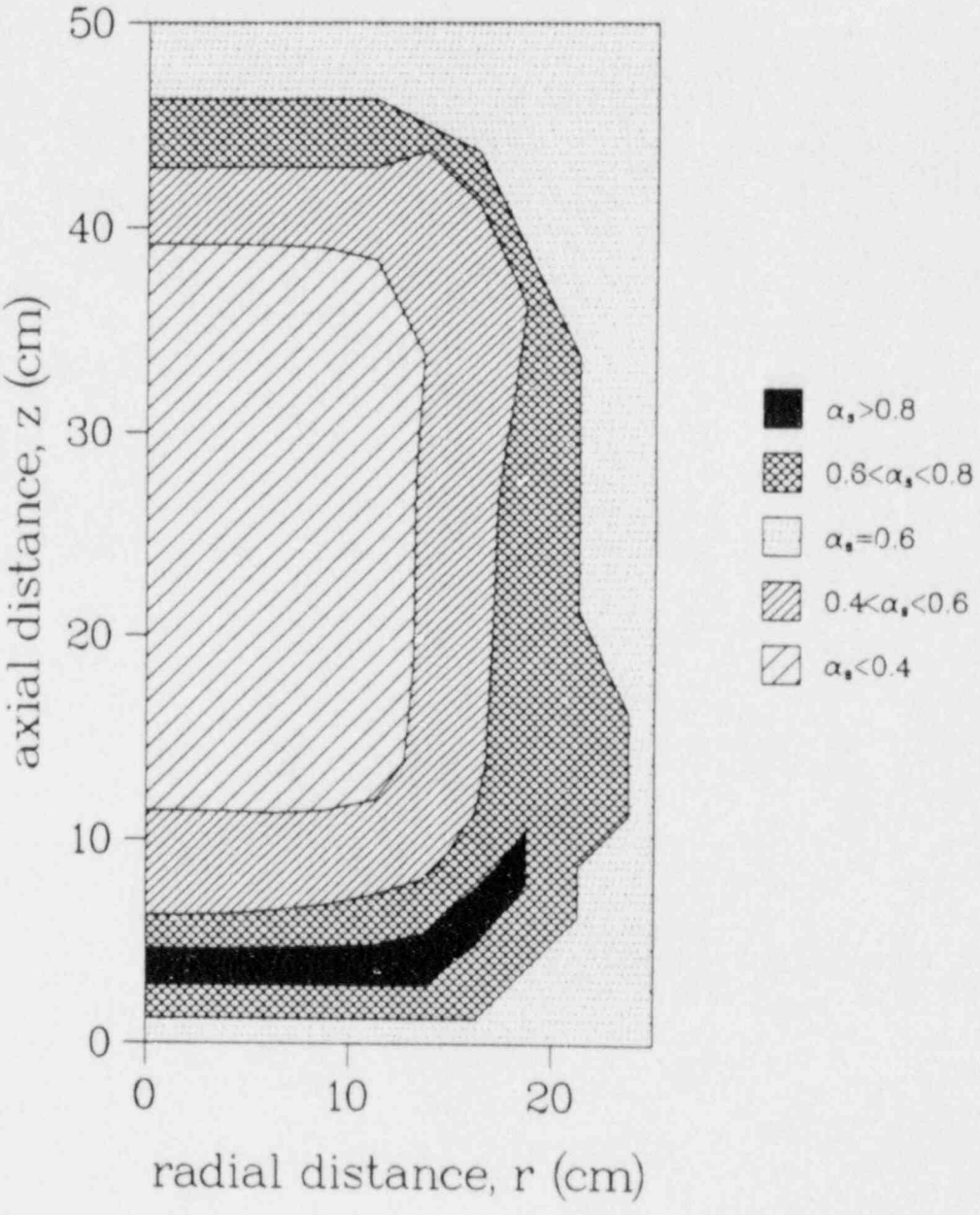

FIG. 10: Solid volume fraction α_s in rubble bed at t=4000 s for the base case. The rubble has an initial uniform solid volume fraction of 0.6.

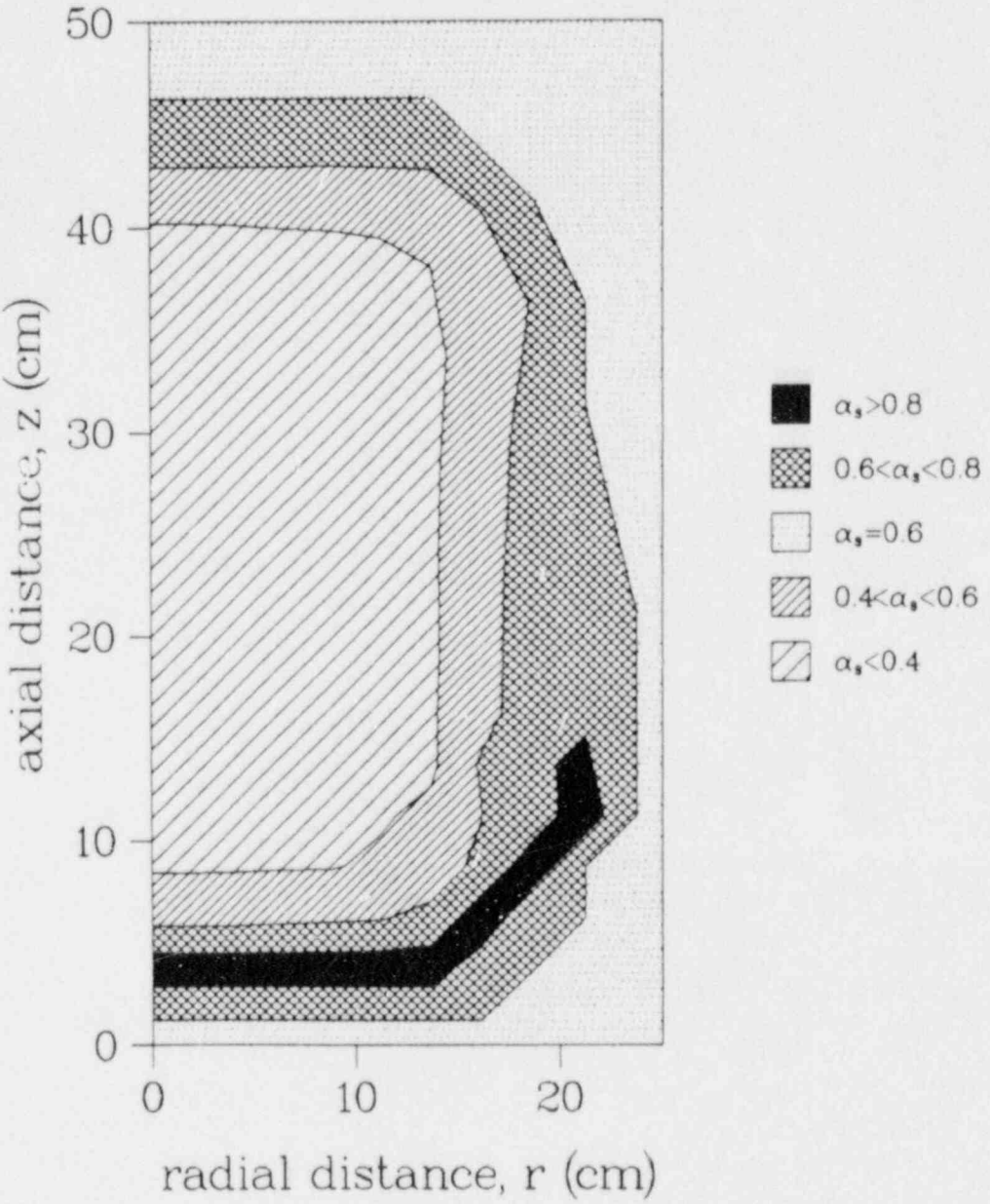

FIG. 11: Solid volume fraction α_s in rubble bed at t=4200 s for the base case. The rubble has an initial uniform solid volume fraction of 0.6.

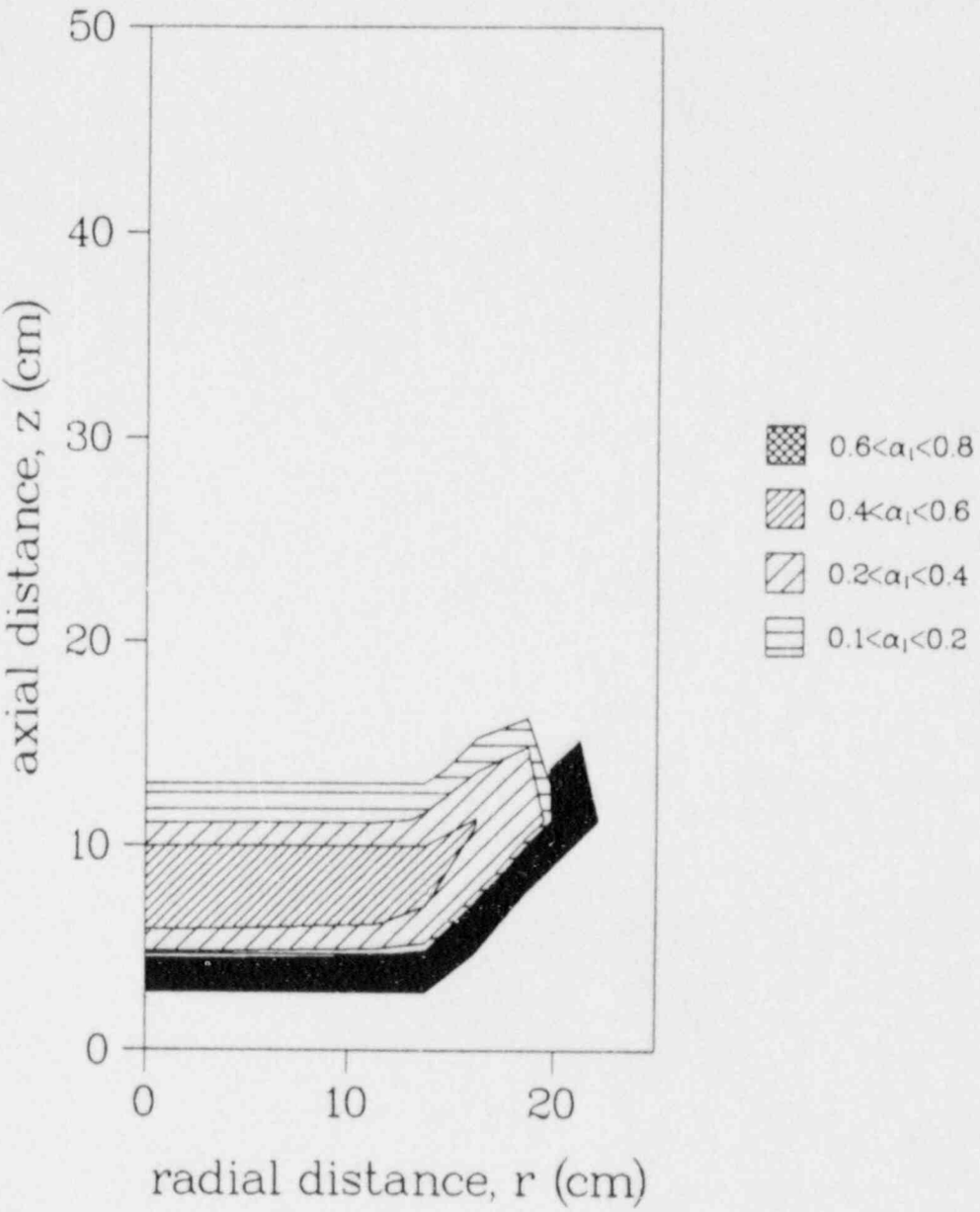

FIG. 12: Liquid volume fraction α_l and the blockage region (in black) at t=4200 s for the base case.

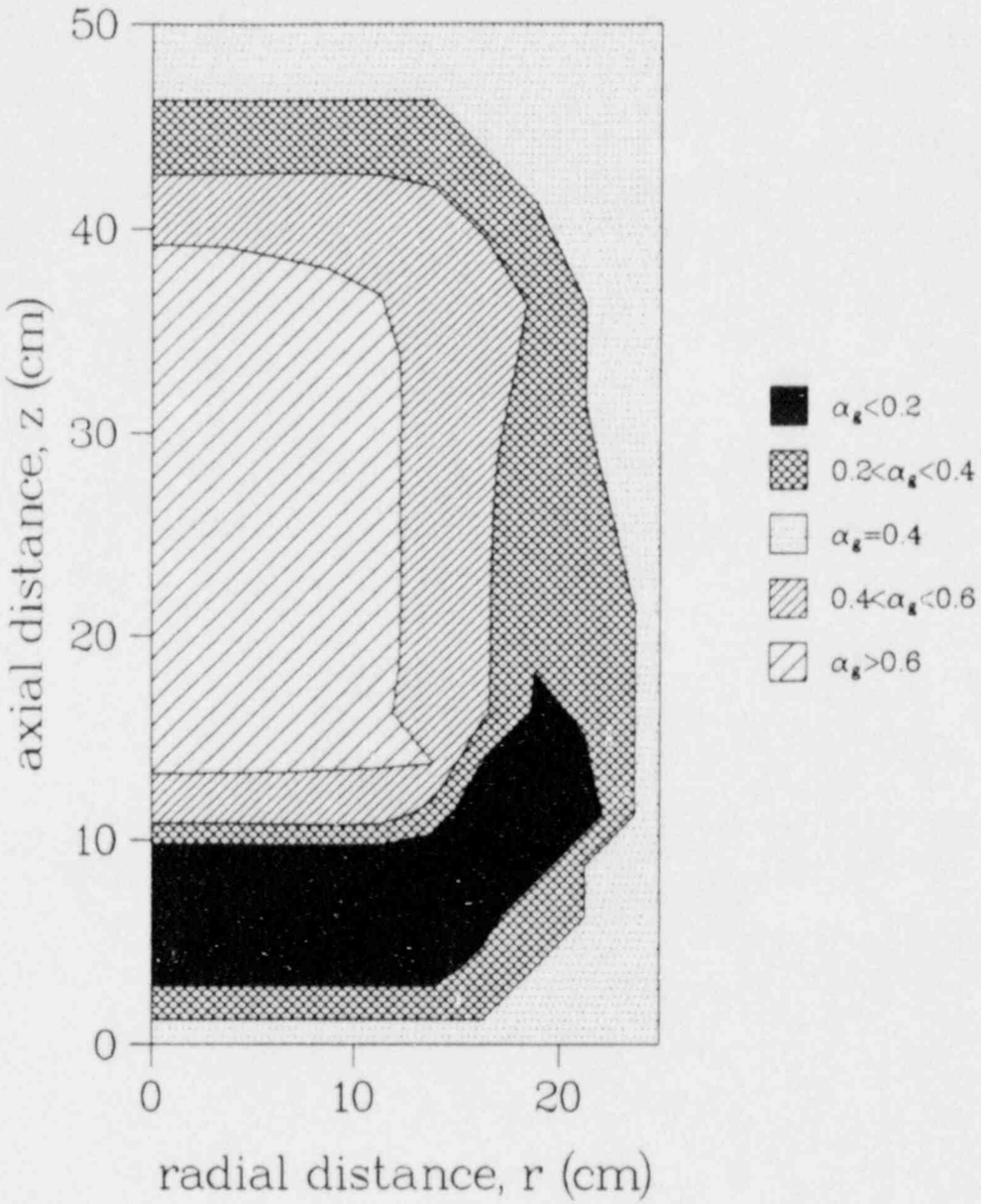

FIG. 13: Gas volume fraction α_g in rubble bed at t=4200 s
for the base case. The rubble has an initial uniform porosity of 0.4.

saturated (S=1). Because $\alpha_s+\alpha_l=1$ in the pool, variations of α_l in Fig.12 are attributable to changes in α_s.

The porosity in the center of the bed reaches 0.7 at t=4200 s and the solid begins settling downward. As is seen from Fig. 14, the temperature of the upper crust at 4200 s is below the solidus temperature. In the current calculation it is assumed that this crust can support the small amount of debris resting above it. Solid, liquid and gas volume fraction profiles at 4400 s are shown in Figs. 15,16 and 17, respectively. A voided region has formed below the upper crust. In portions of the molten pool the solid volume fraction has decreased below 0.4 and the liquid volume fraction has increased above 0.6 (recall that $\alpha_s+\alpha_l=1$ in the pool).

Solid, liquid and gas volume fraction profiles at 4600 s are shown in Figs. 18,19 and 20, respectively. As the high porosity solid in the center continues to settle downward, the size of the voided region increases. At t=4600 s, this zone is 10 cm high and 11 cm in radius. Note that changes in the critical solid fraction $\alpha_{s,min}$ will affect the growth of the voided region. Experiments are needed to evaluate the current bed collapse model and suggest possible improvements.

Zirconia and Urania melt fractions are plotted as functions of time in Figs. 21 and 22, respectively. Also shown are the fractions that have refrozen to form the crust. Solid begins melting at 3080 s and liquid starts refreezing soon after motion is first observed ($\simeq$3300 s). At t=4500 s, a third of the ZrO_2 has undergone a phase change and almost sixty percent of the liquid ZrO_2 has refrozen. Only twelve percent of the UO_2 has melted, of which a small fraction ($\simeq$18%) has refrozen. A greater portion of the ZrO_2 has melted because the concentration of ZrO_2 in the liquid is initially larger than in the solid. This effect becomes less pronounced as time passes. As the ZrO_2 is depleted, the rate at which UO_2 melts increases rapidly while the rate of ZrO_2 melt formation levels off. Because the bulk of the crust is formed early in the meltdown sequence, a large fraction of the ZrO_2 refreezes.

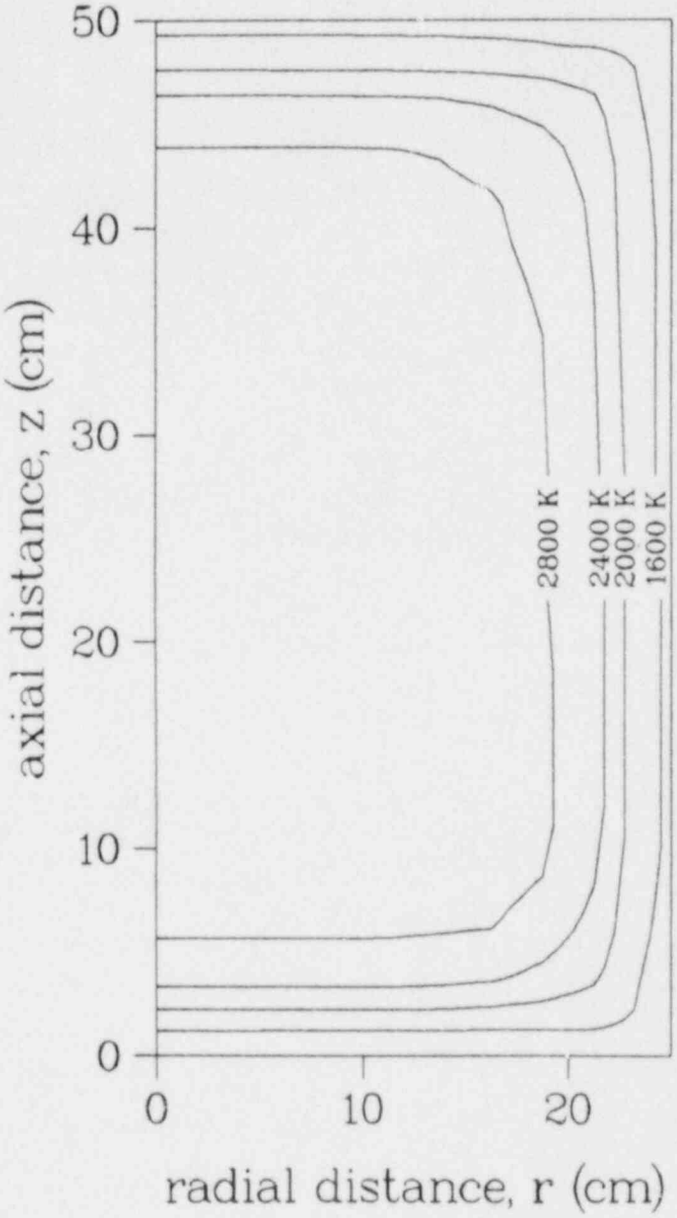

FIG. 14: Temperature contours in rubble bed at t=4200 s for the base case. Contours are shown every 400 K.

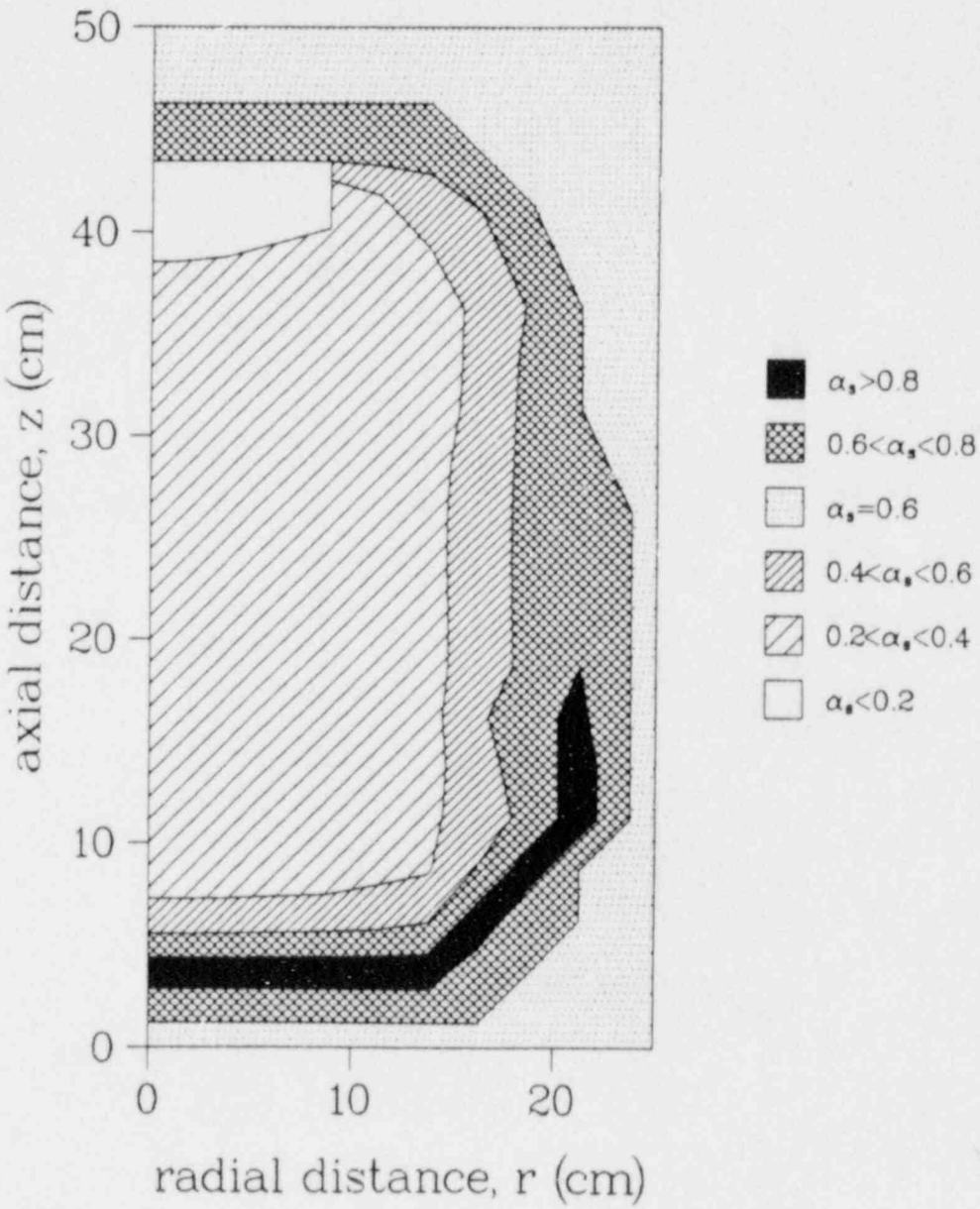

FIG. 15. Solid volume fraction α_s in rubble bed at t=4400 s for the base case. The rubble has an initial uniform solid volume fraction of 0.6.

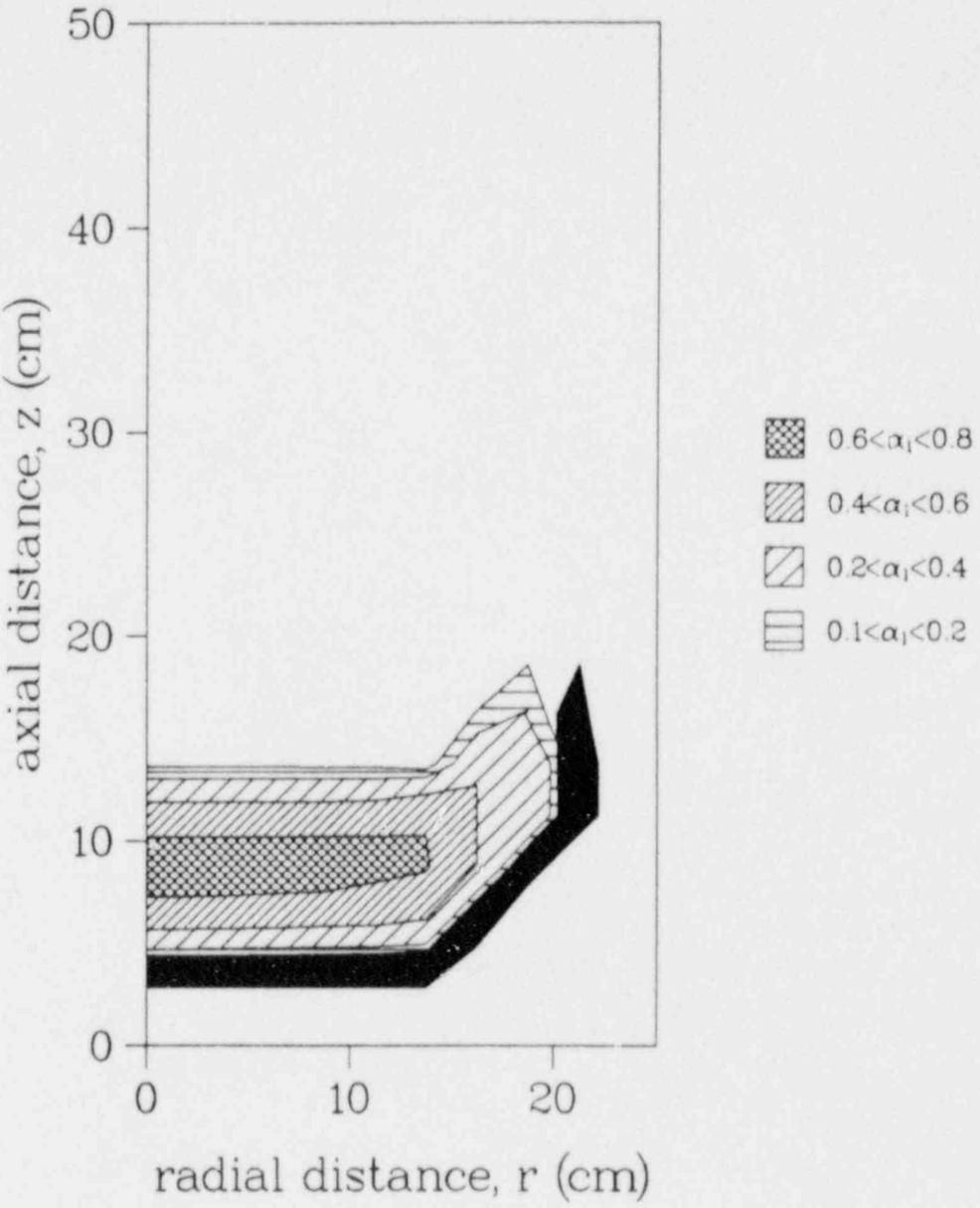

FIG. 16: Liquid volume fraction α_l and the blockage region (in black) at t=4400 s for the base case.

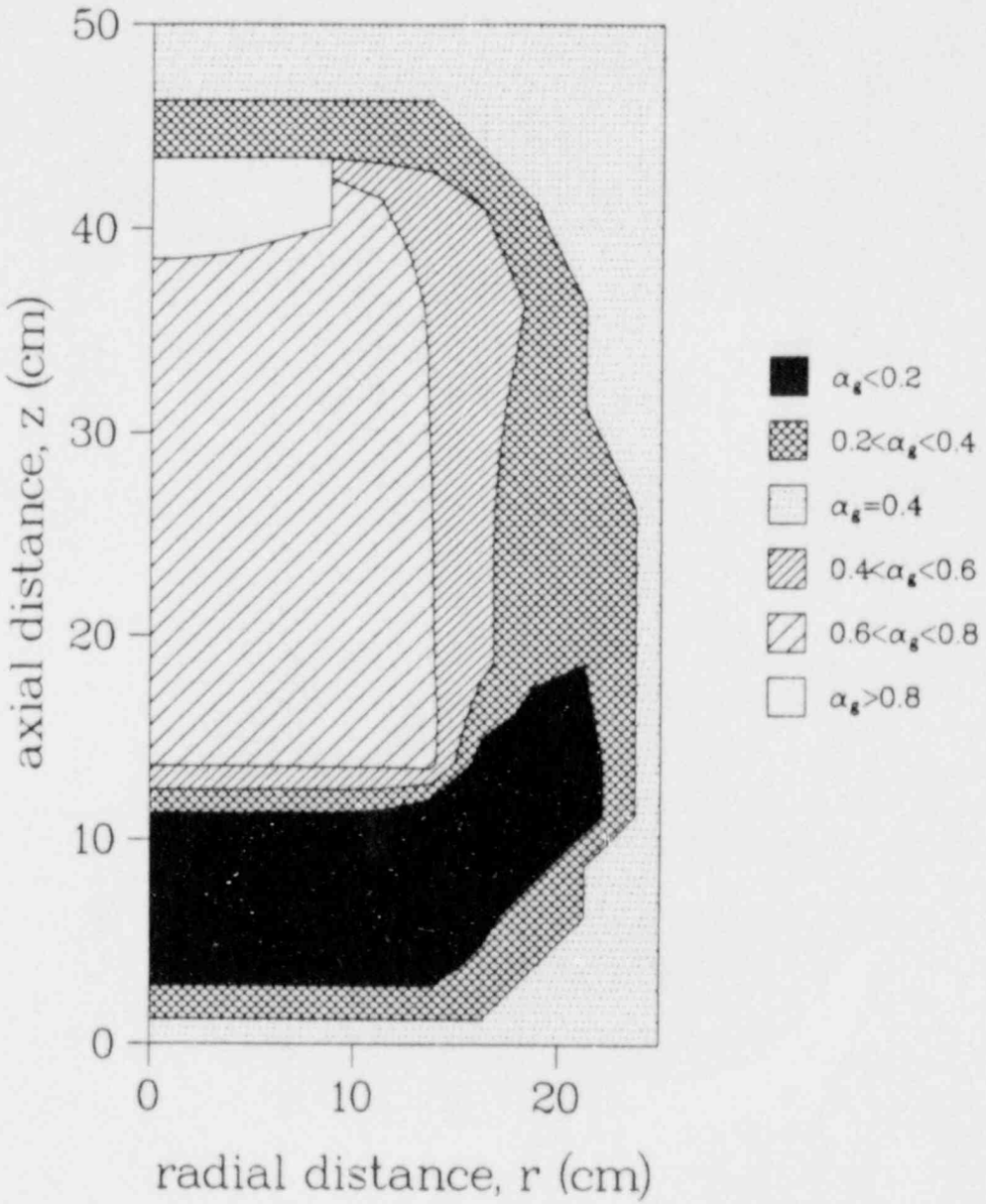

FIG. 17: Gas volume fraction α_g in rubble bed at t=4400 s for the base case. The rubble has an initial uniform porosity of 0.4.

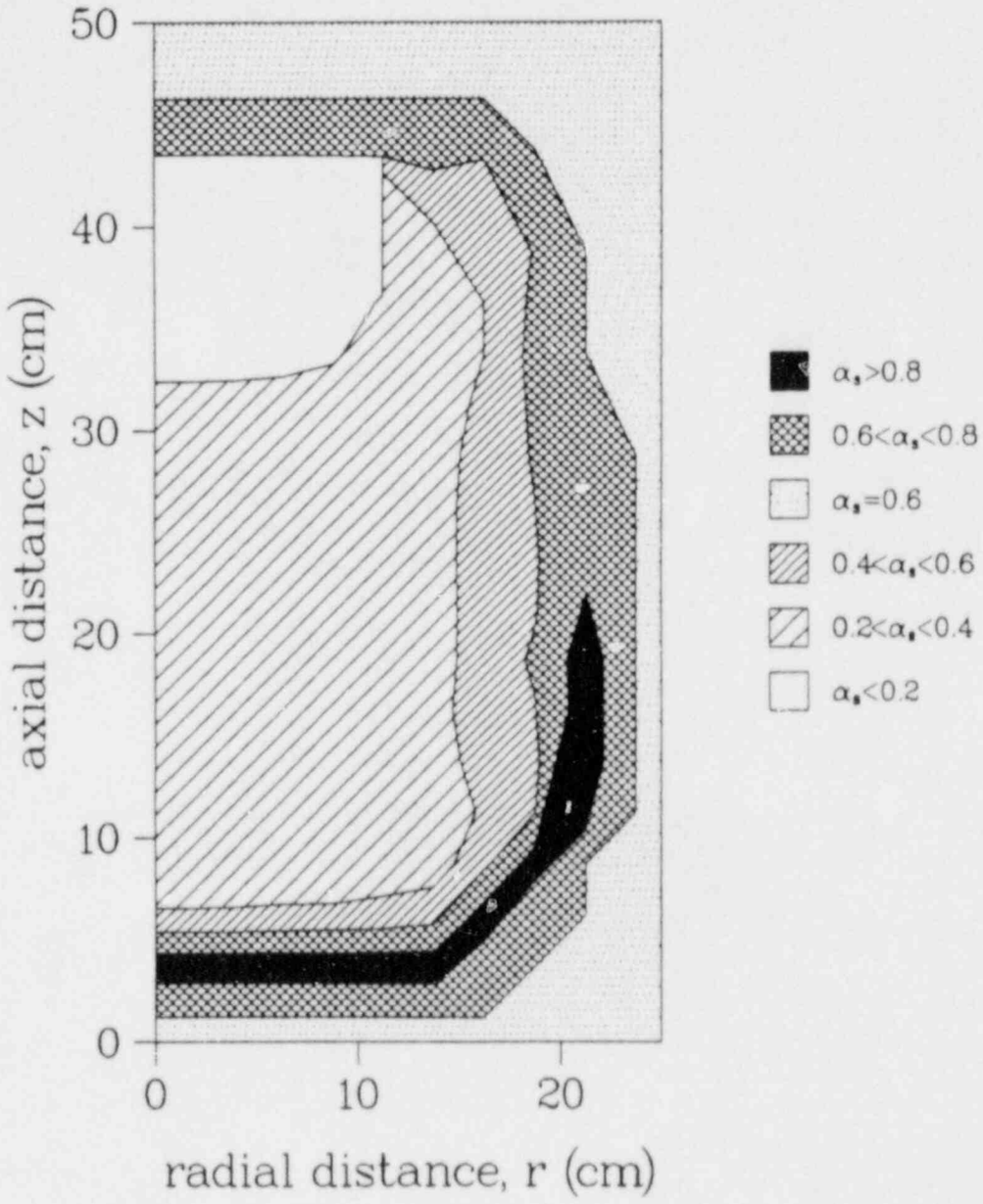

FIG. 18: Solid volume fraction α_s in rubble bed at t=4600 s for the base case. The rubble has an initial uniform solid volume fraction of 0.6.

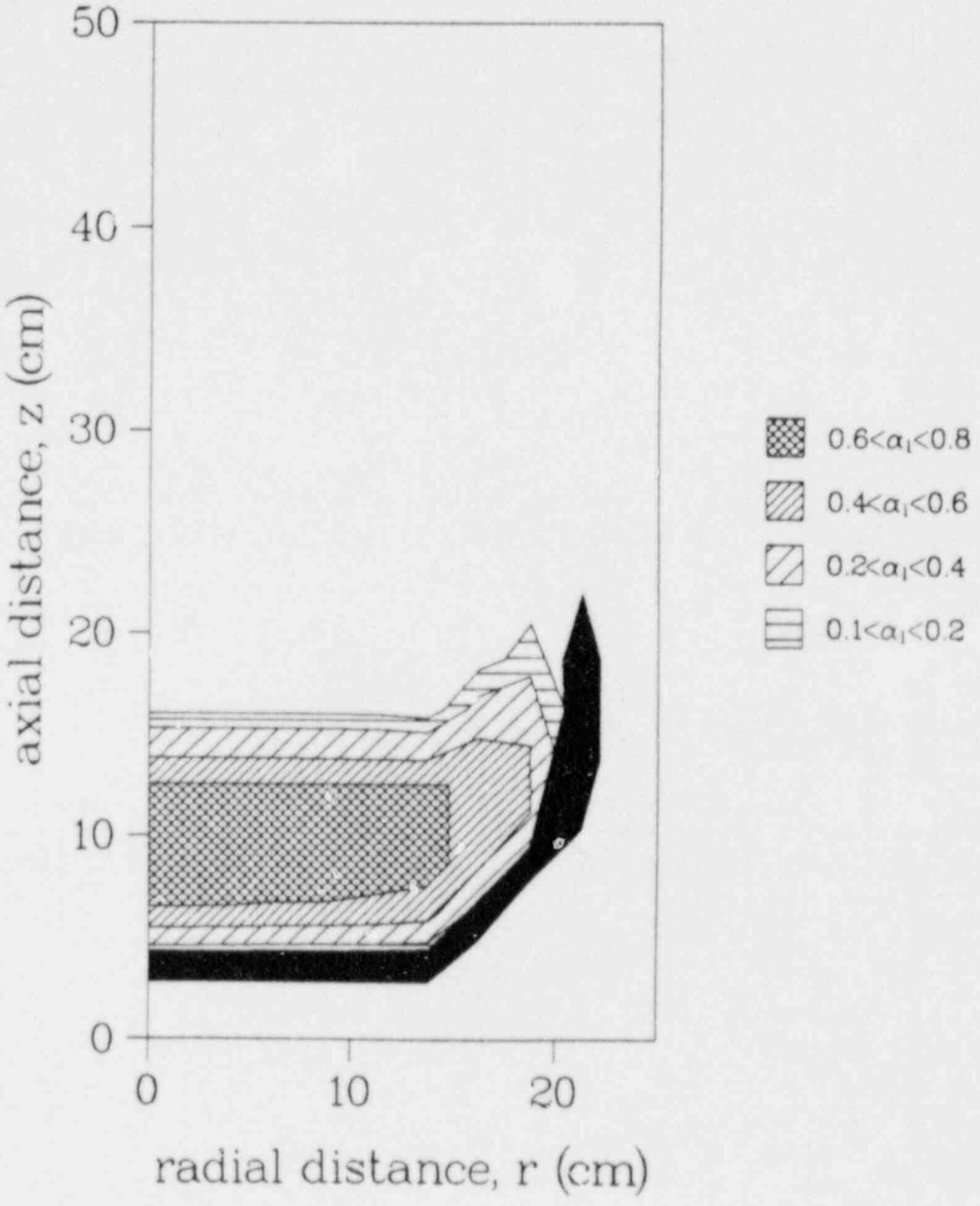

FIG. 19: Liquid volume fraction α_l and the blockage region (in black) at t=4600 s for the base case.

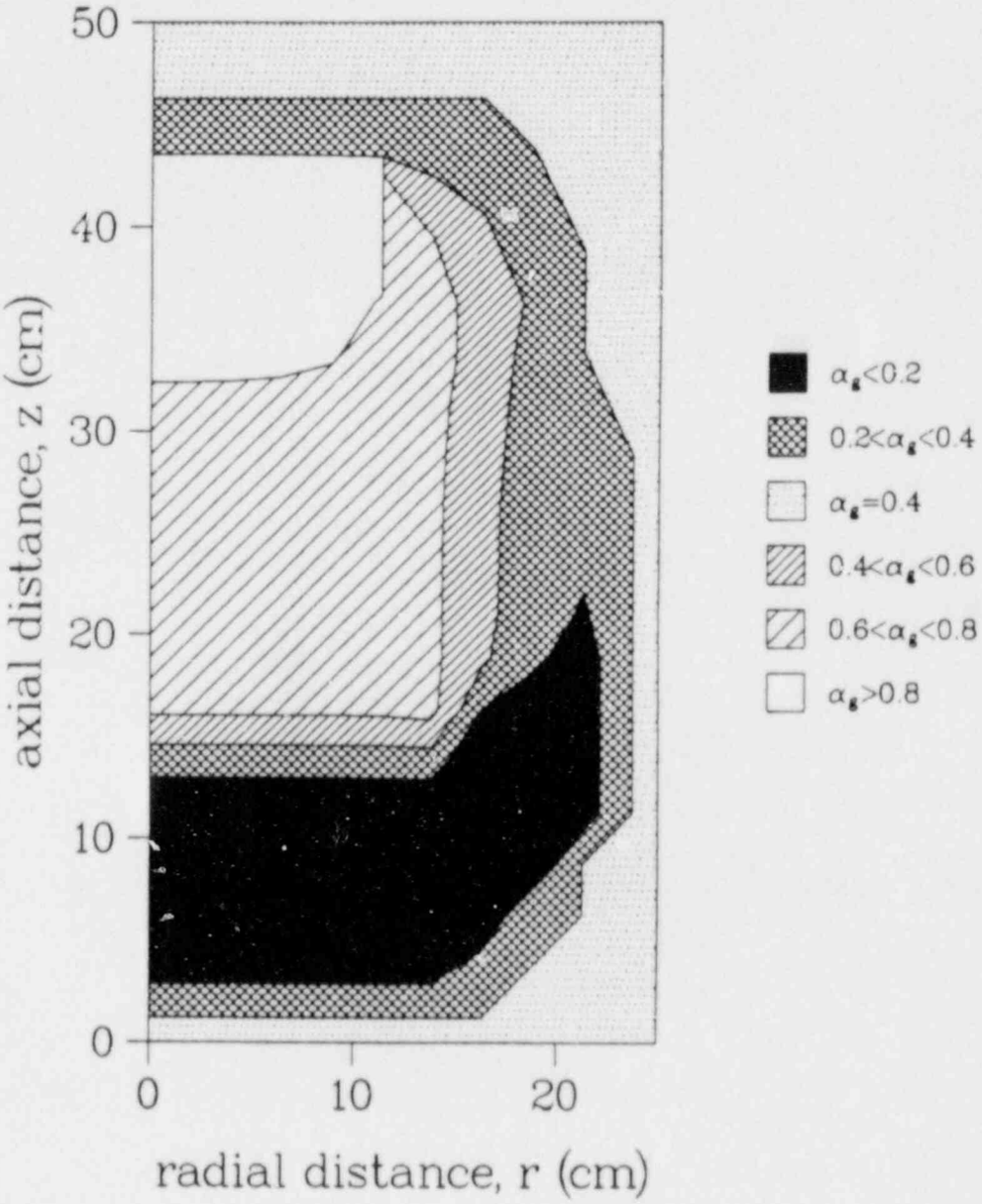

FIG. 20: Gas volume fraction α_g in rubble bed at t=4600 s for the base case. The rubble has an initial uniform porosity of 0.4.

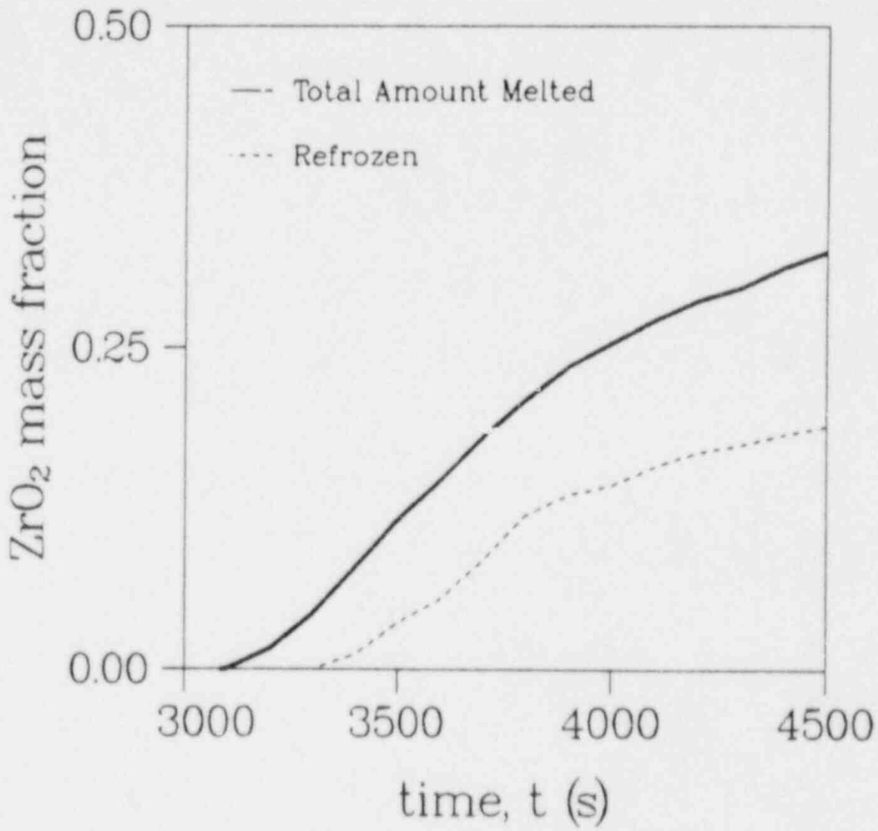

FIG. 21: Fraction of the ZrO_2 that has melted (solid line) and the fraction that has melted and refrozen (dashed line).

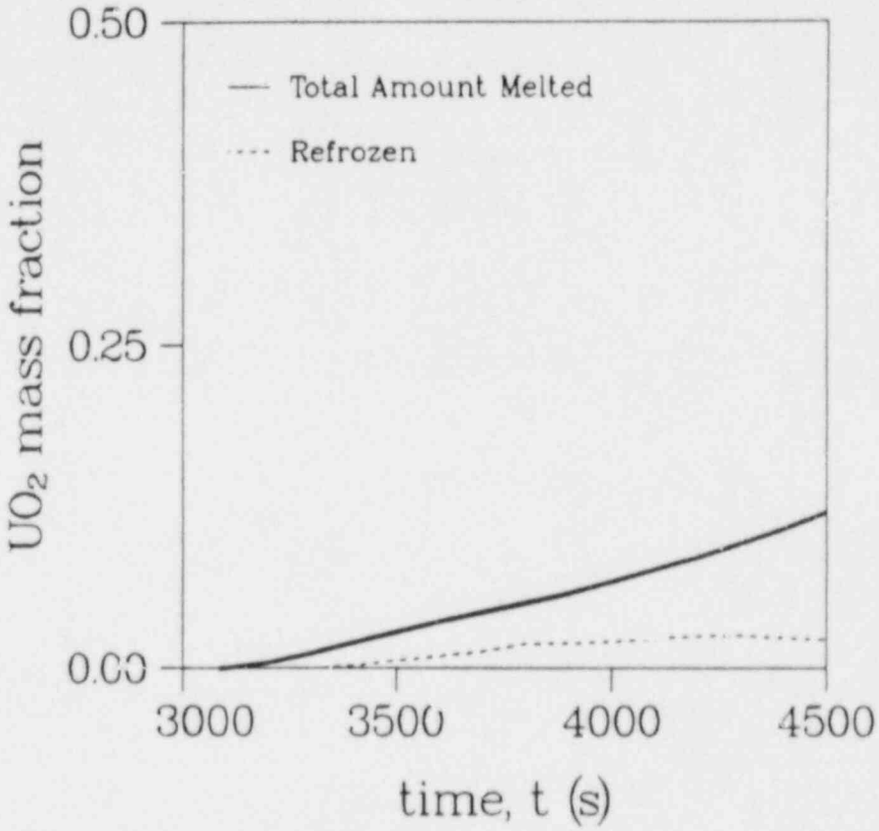

FIG. 22: Fraction of the UO_2 that has melted (solid line) and the fraction that has melted and refrozen (dashed line).

8.2 Effect of Varying the Particle Diameter

Solutions are presented in this section for a bed composed of 5 mm diameter particles. Parameters such as the initial and boundary conditions, the size of the bed and the composition, are kept fixed at their base case values. Solid volume fractions are shown every two hundred seconds from 3200 s to 4200 s in Figs. 23 through 28. Increasing d_p enhances radiation transfer through the bed, raising both the effective thermal conductivity and the thermal boundary layer thickness. Consequently, in beds composed of large particles, blockages form further from the boundaries, the solid starts melting later and the melt zone is smaller. These effects may have a bearing on the decision to add water to the reactor vessel during an accident if it is suspected that the rods might fragment into fine particulate when quenched.

Comparing Figs. 4 and 24 it is evident that the lower crust is initially thicker for a bed composed of 5 mm particles. In beds with large particles, melt relocation is faster (the permeability is proportional to d_p^2) and liquid starts moving earlier because the critical residual saturation is lower ($S_r \sim 1/d_p$). Liquid quickly flows out of the melt zone as it forms and refreezes in colder portions of the bed. Consequently, refreezing is much more vigorous in beds with large d_p and the initial crusts are larger.

Note that the capillary rise discussed in the previous section is less evident in Fig. 29 than in Figs. 12, 16 and 19. This is due to the fact that capillary forces are less important in beds with large particles (recall that the capillary pressure is inversely proportional to particle diameter).

Phase volume fraction profiles at 4400 s and at 4600 s are shown in Figs. 30-32 and Figs. 33-35, respectively. Debris starts settling before 4800 s elapse - see Figs. 36 and 37. In the bed with 1 mm diameter particles, a crust was created above the melt zone early in the meltdown sequence and a void formed above the melt zone as solid collapsed downward (see Fig.11). Such an upper crust does not form in the bed with d_p=5 mm because capillary forces are weaker.

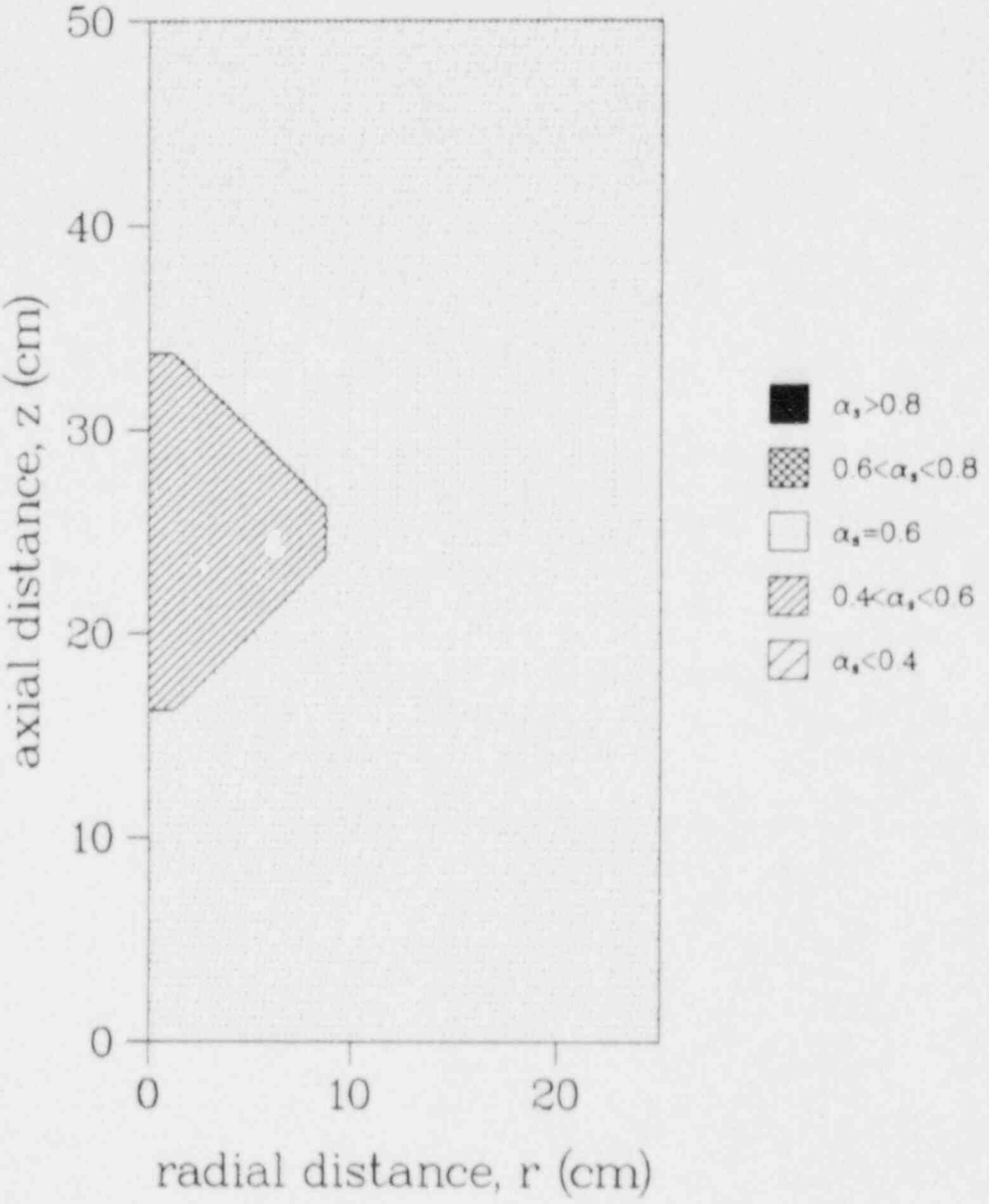

FIG. 23 Solid volume fraction α_s in rubble bed at t=3200 s for a bed with an average pa. .cle diameter of 5 mm. The rubble has an initial uniform solid volume fraction of 0.6.

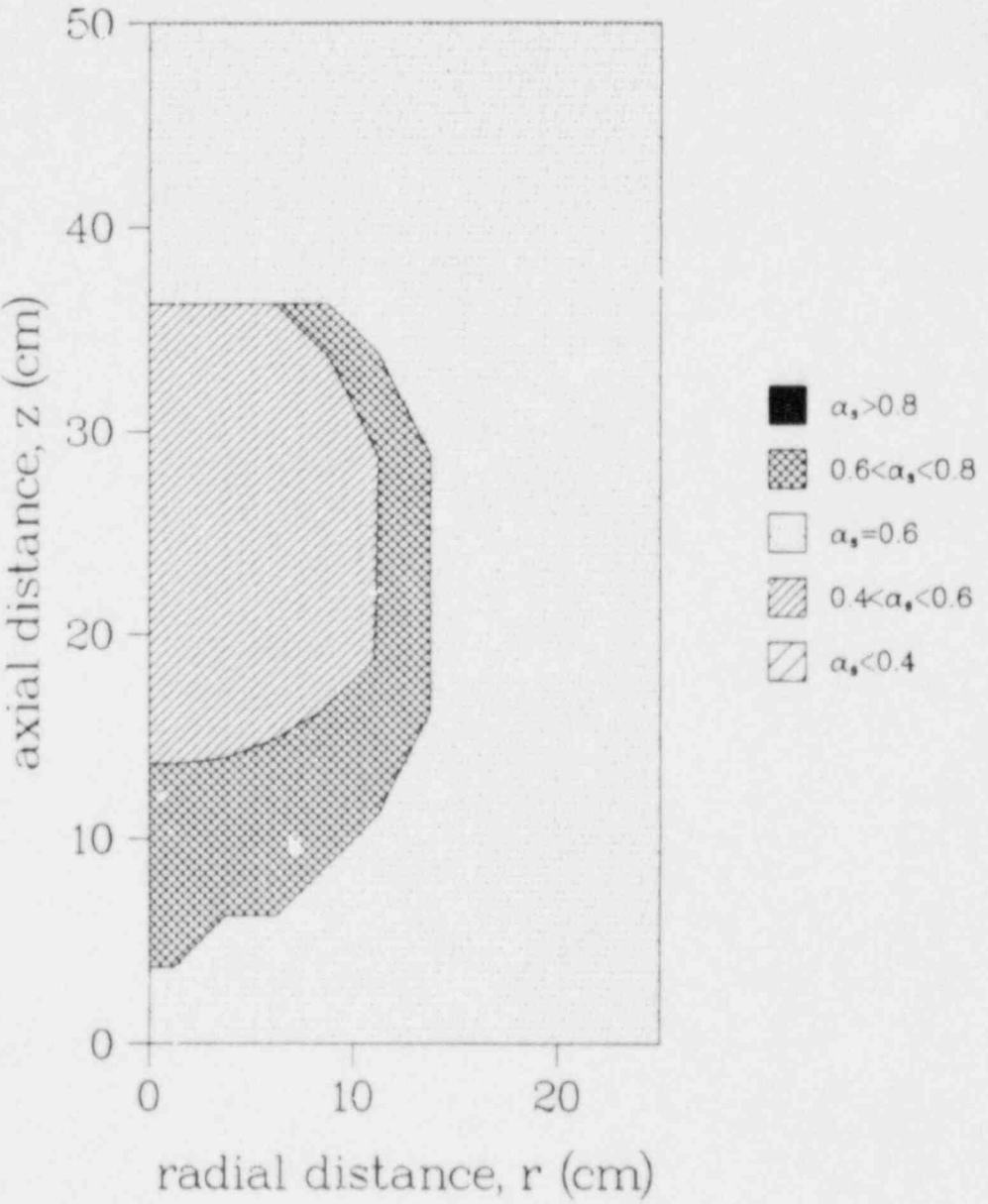

FIG. 24: Solid volume fraction α_s in rubble bed at t=3400 s for a bed with an average particle diameter of 5 mm. The rubble has an initial uniform solid volume fraction of 0.6.

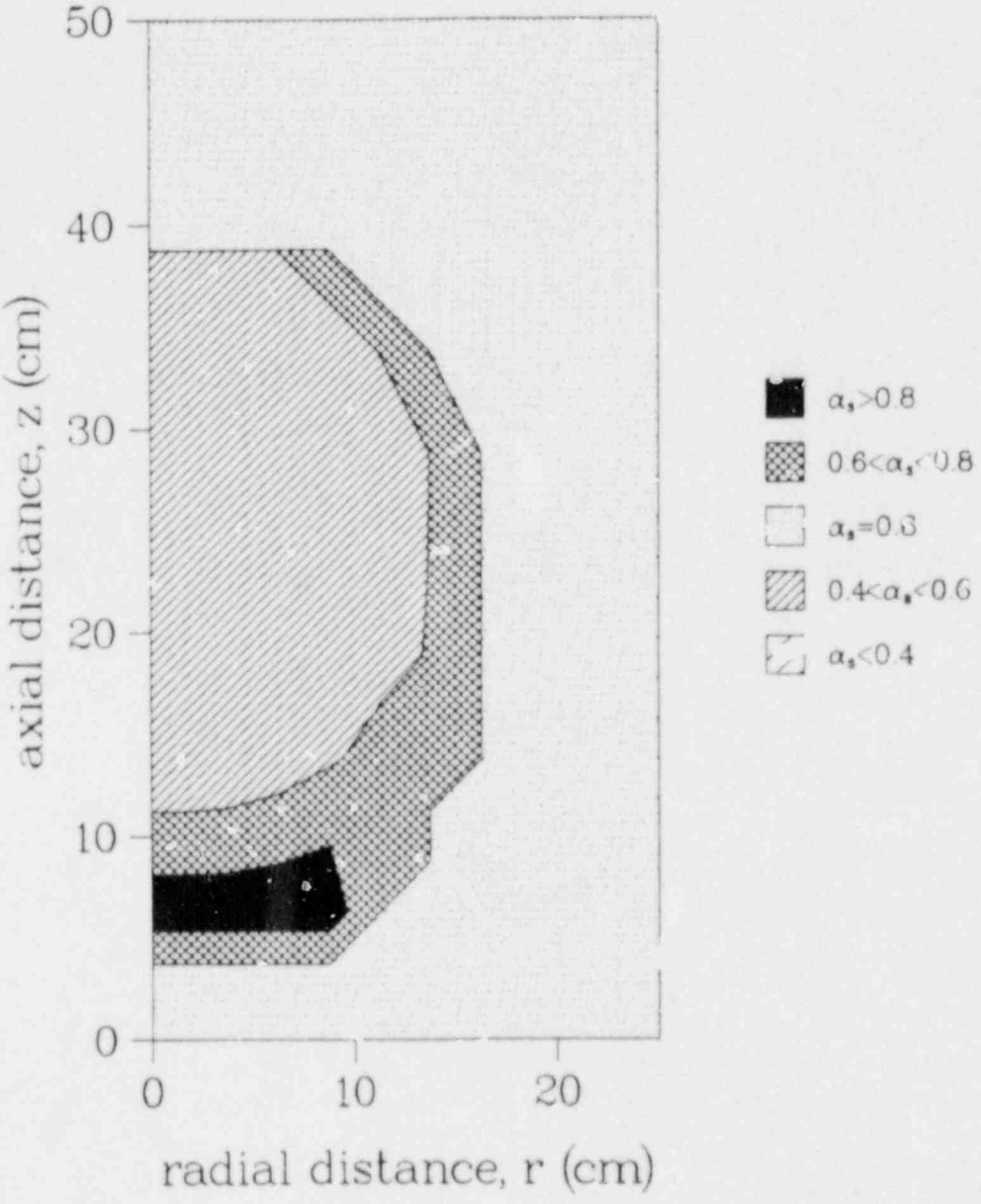

FIG 25: Solid volume fraction α_s in rubble bed at t=3600 s for a bed with an average particle diameter of 5 mm. The rubble has an initial uniform solid volume fraction of 0.6.

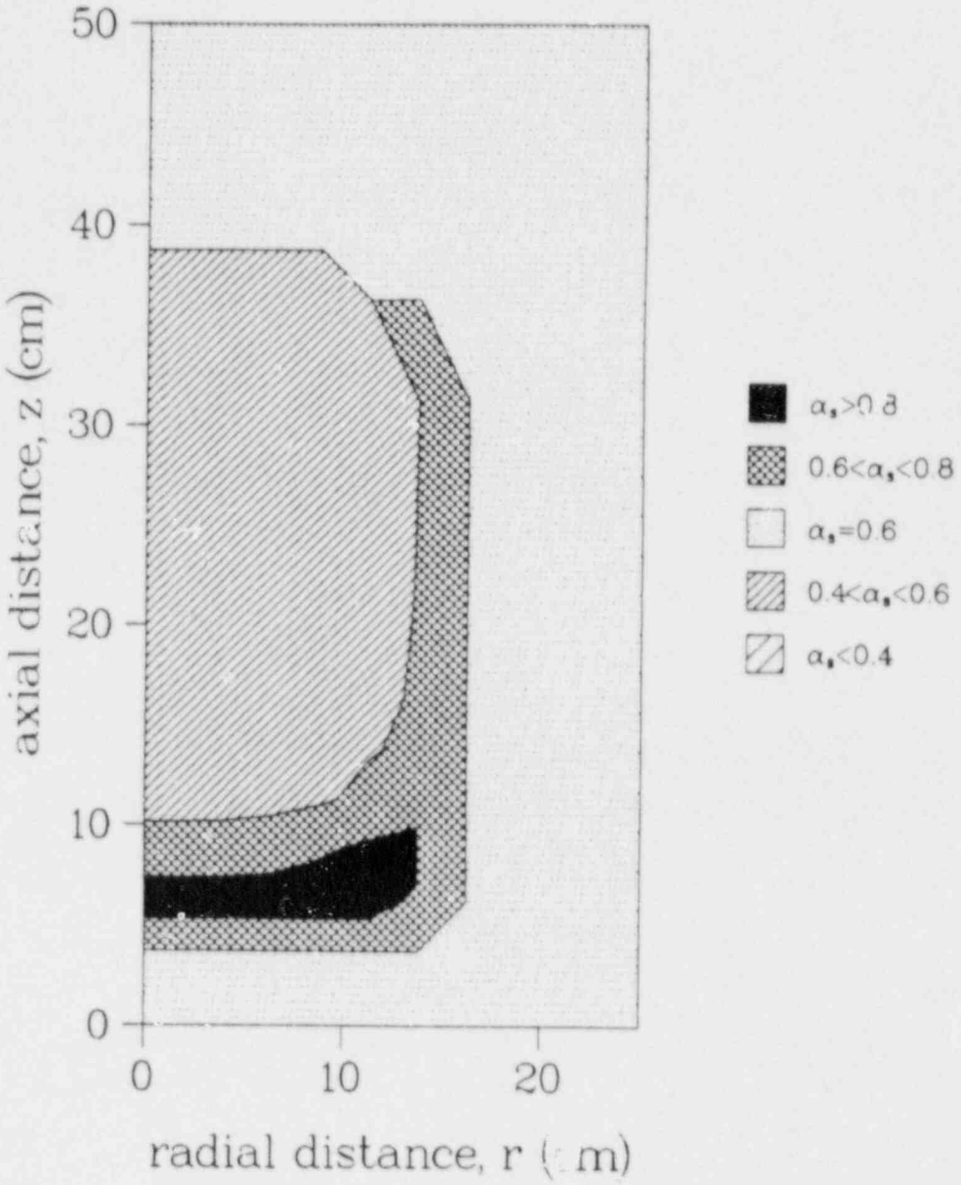

FIG. 26: Solid volume fraction α_s in rubble bed at t=3800 s for a bed with an average particle diameter of 5 mm. The rubble has an initial uniform solid volume fraction of 0.6.

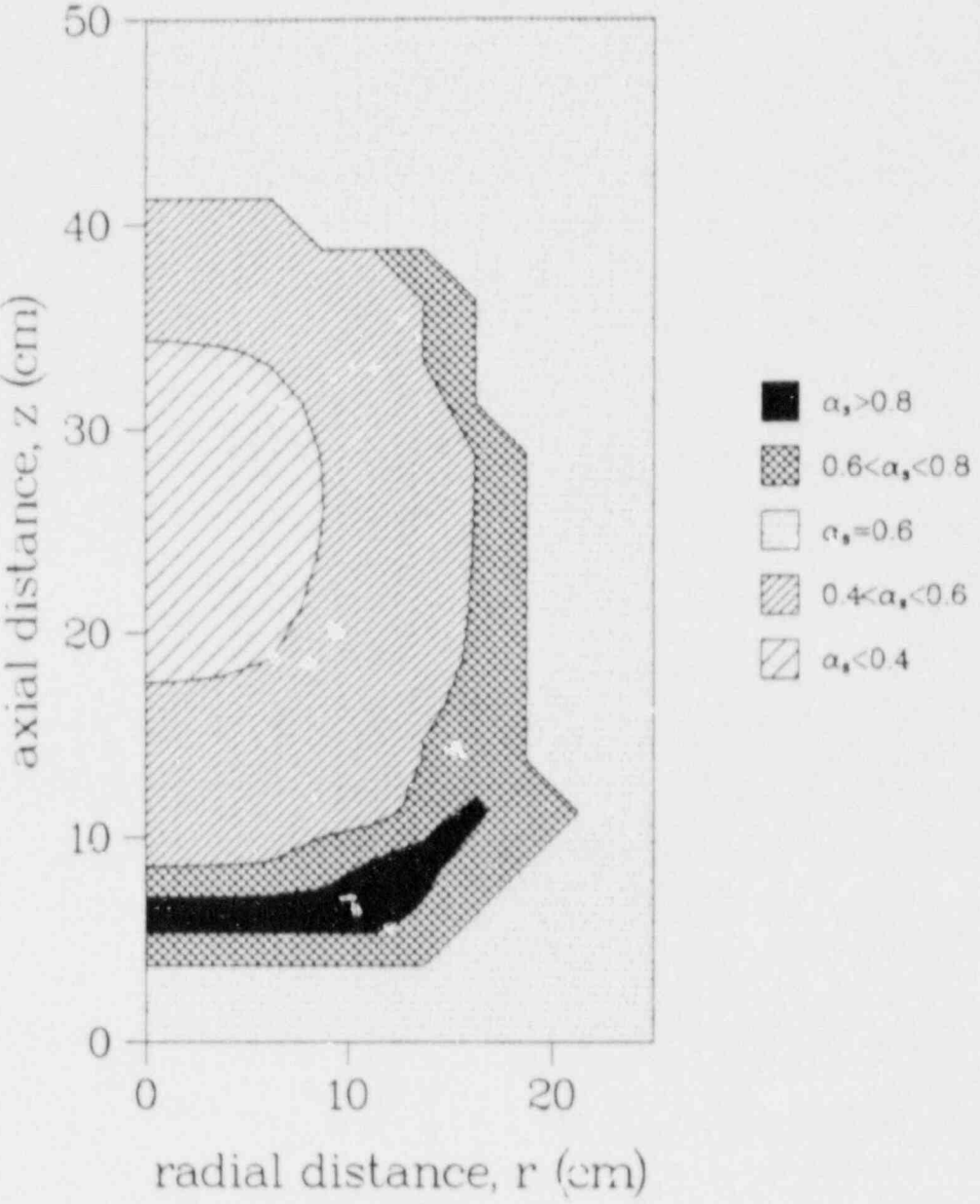

FIG 27: Solid volume fraction α_s in rubble bed at t=4000 s for a bed with an average particle diameter of 5 mm. The rubble has an initial uniform solid volume fraction of 0.6.

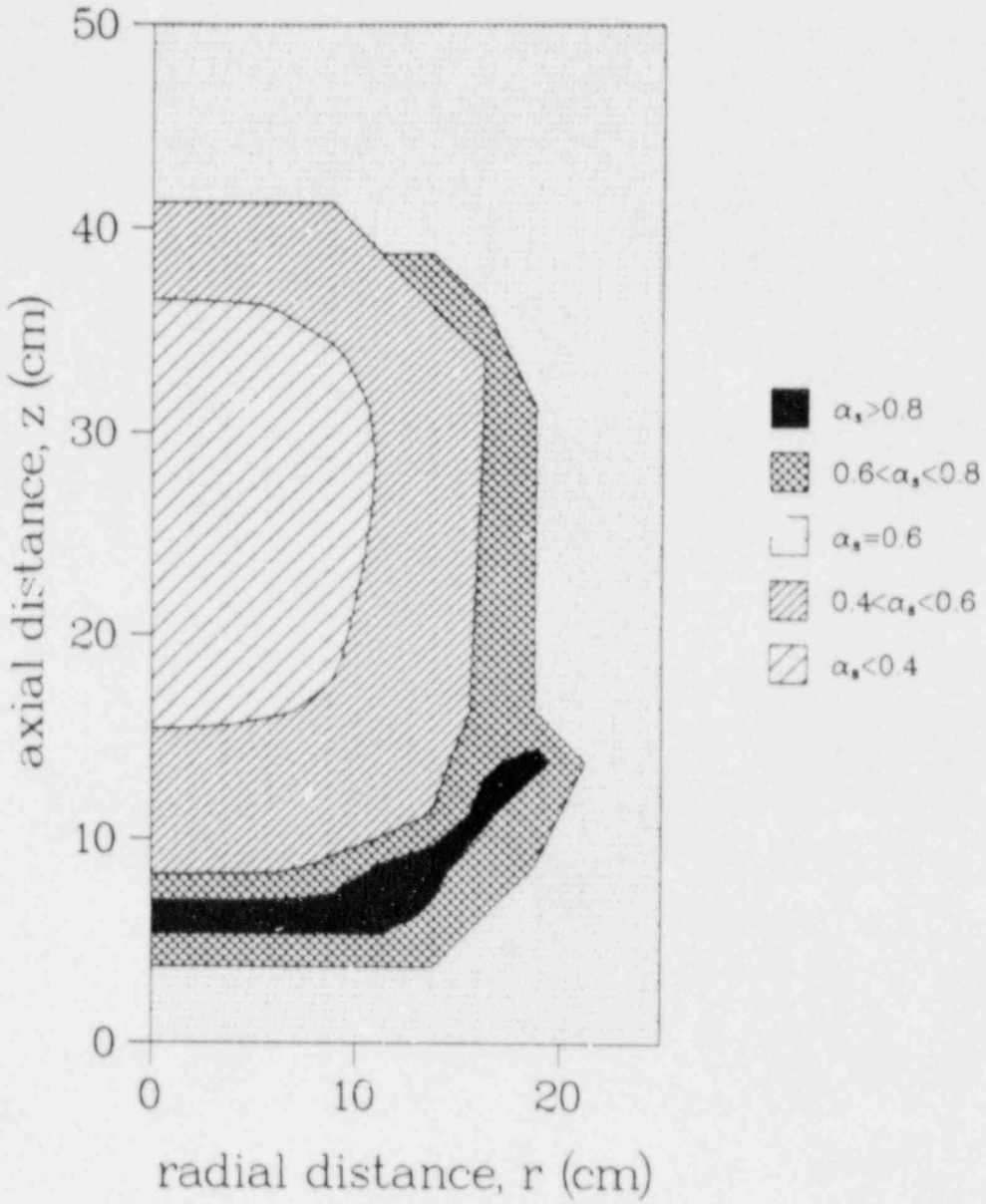

FIG. 28: Solid volume fraction α_s in rubble bed at t=4200 s for a bed with an average particle diameter of 5 mm. The rubble has an initial uniform solid volume fraction of 0.6.

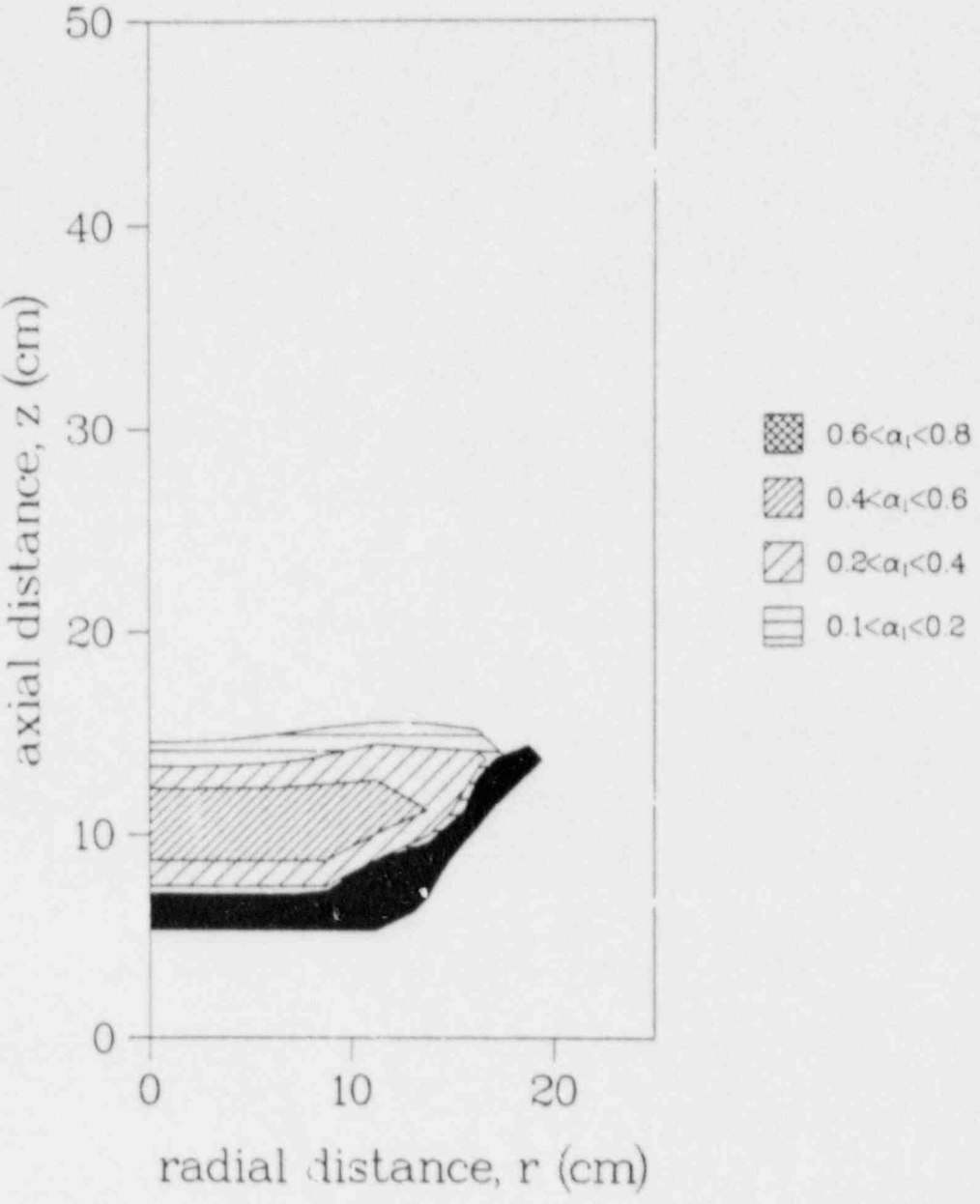

FIG. 29: Liquid volume fraction α_l and the blockage region (in black) at t=4200 s for a bed with 5 mm diameter particles.

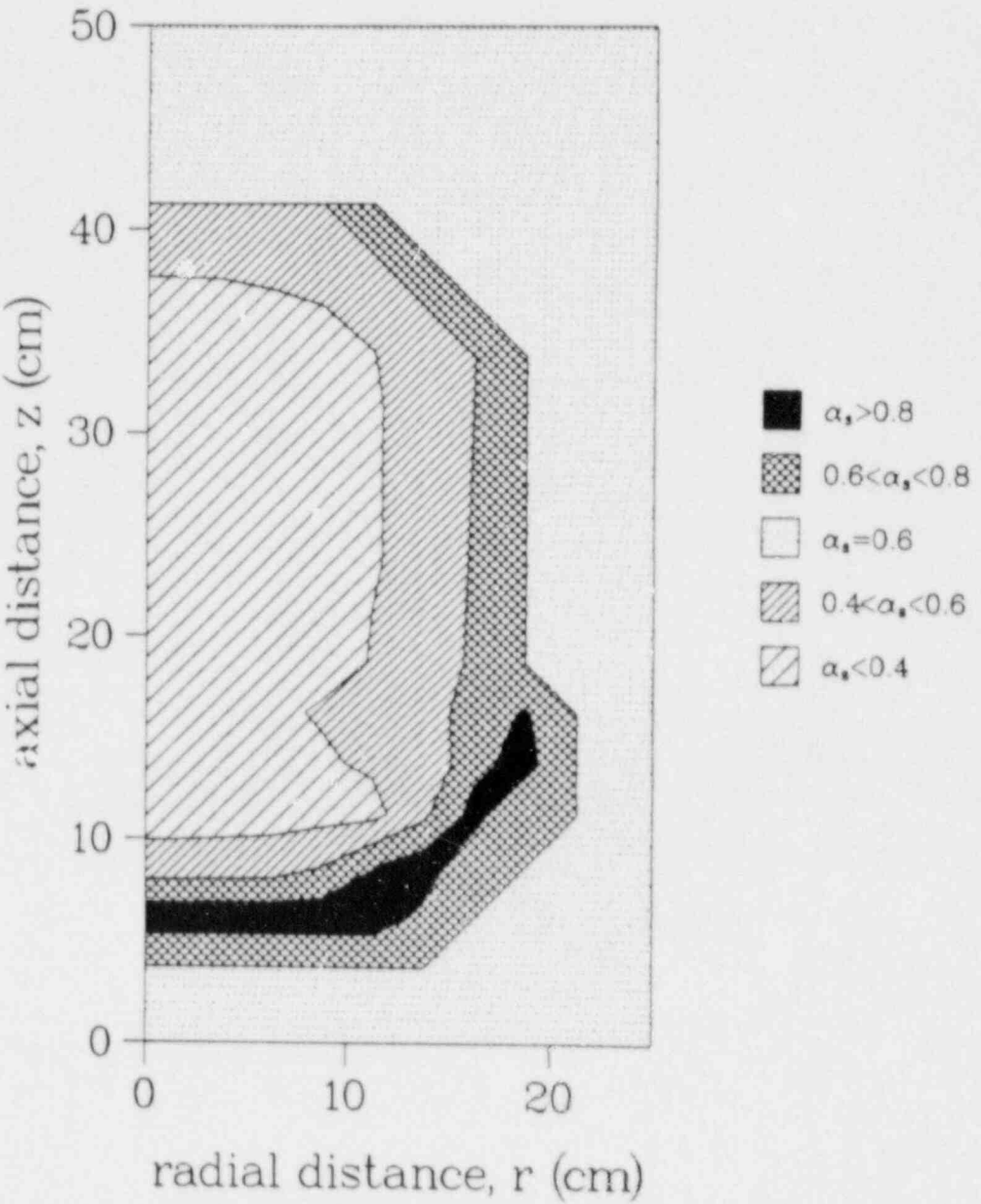

FIG. 30: Solid volume fraction α_s in rubble bed at t=4400 s for a bed with an average particle diameter of 5 mm. The rubble has an initial uniform solid volume fraction of 0.6.

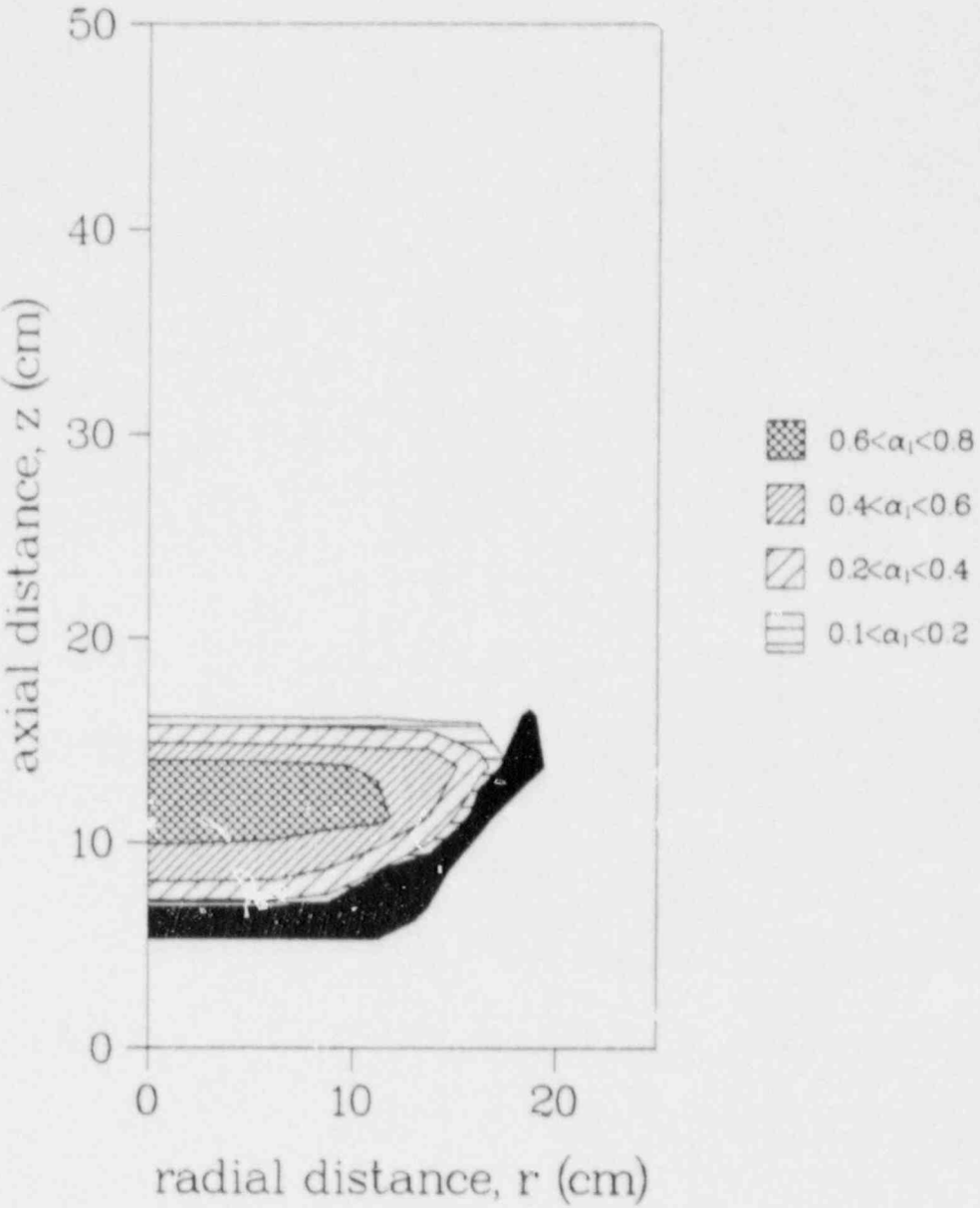

FIG. 31. Liquid volume fraction α_l and the blockage region (in black) at t=4400 s for a bed with 5 mm diameter particles.

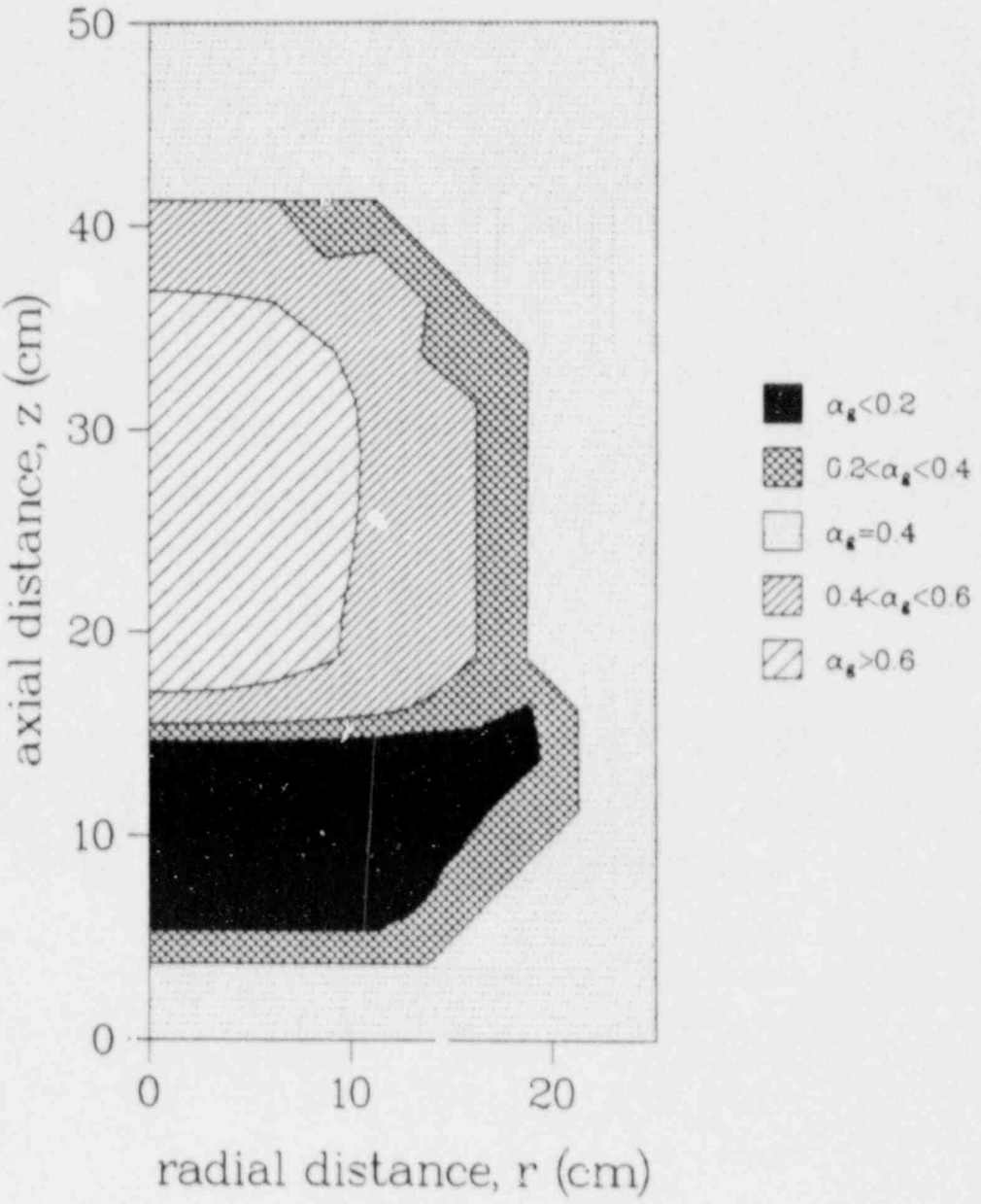

FIG. 32. Gas volume fraction α_g in the rubble bed at t=4400 s for a bed with an average particle diameter of 5 mm. The rubble has an initial uniform porosity of 0.4.

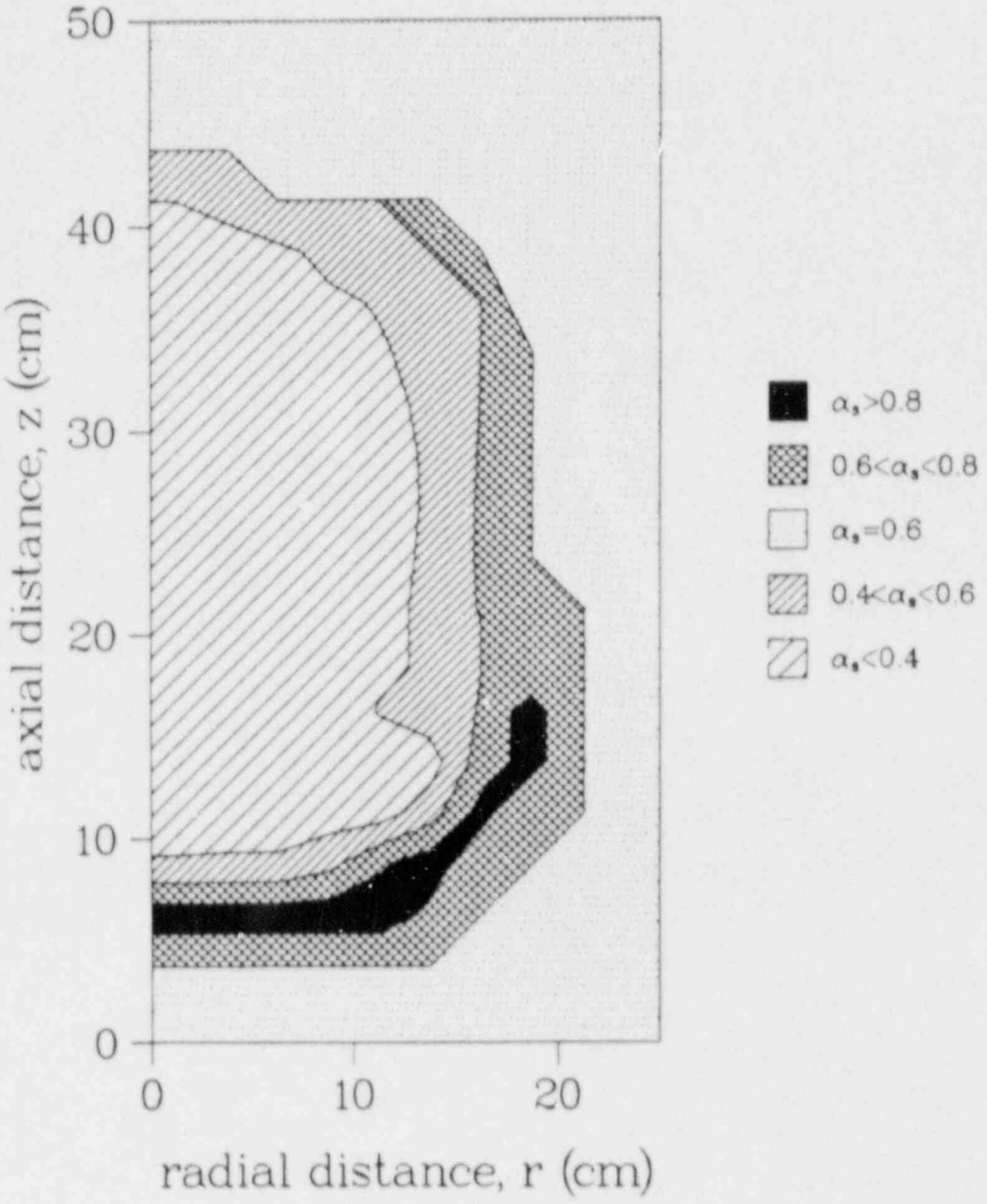

FIG. 33: Solid volume fraction α_s in rubble bed at t=4600 s for a bed with an average particle diameter of 5 mm. The rubble has an initial uniform solid volume fraction of 0.6.

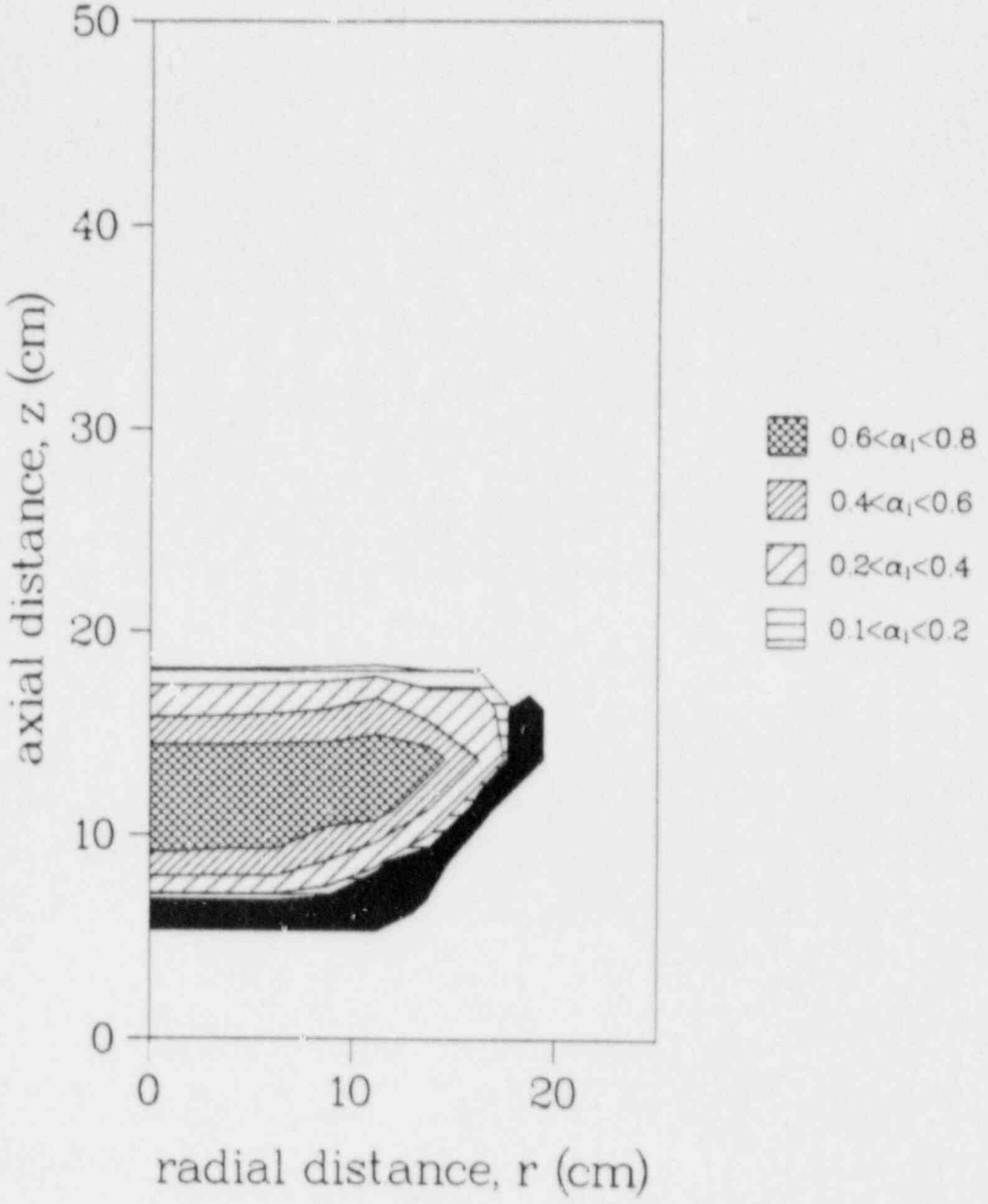

FIG. 34: Liquid volume fraction α_l and the blockage region (in black) at t=4600 s for a bed with 5 mm diameter particles.

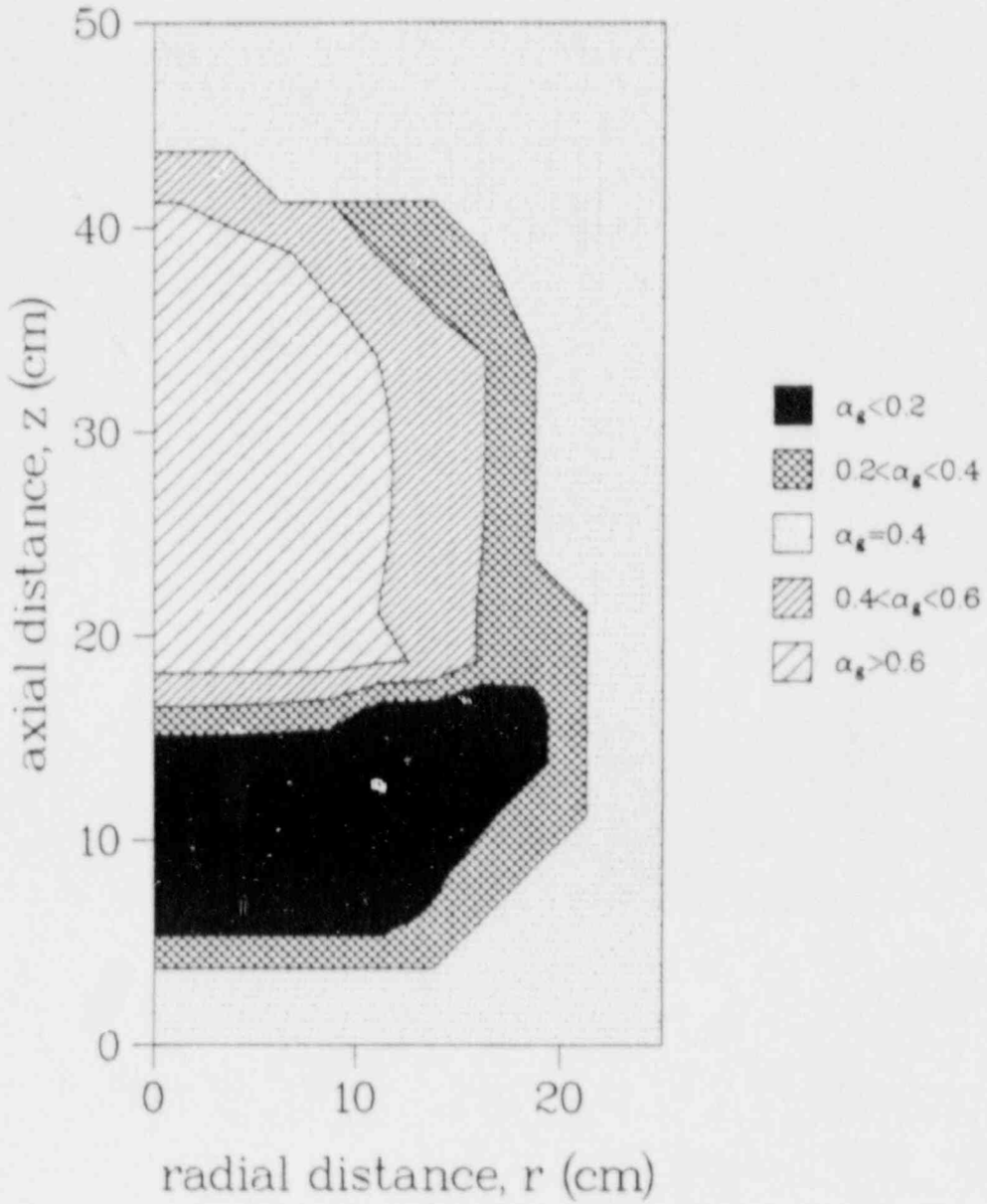

FIG. 35: Gas volume fraction α_g in the rubble bed at t=4600 s for a bed with an average particle diameter of 5 mm. The rubble has an initial uniform porosity of 0.4.

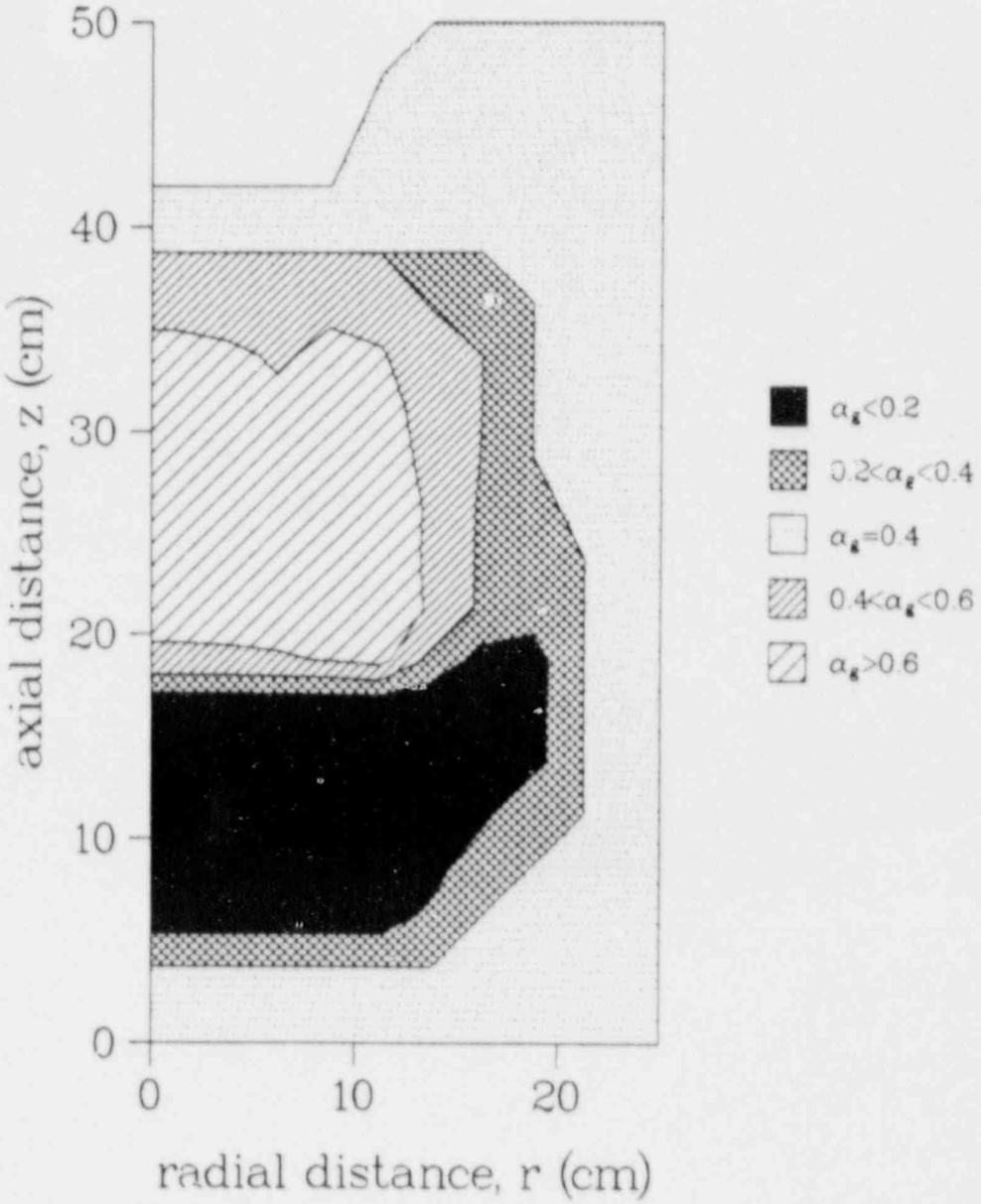

FIG. 36: Gas volume fraction α_g in the rubble bed at t=4800 s for a bed with an average particle diameter of 5 mm. The rubble has an initial uniform porosity of 0.4.

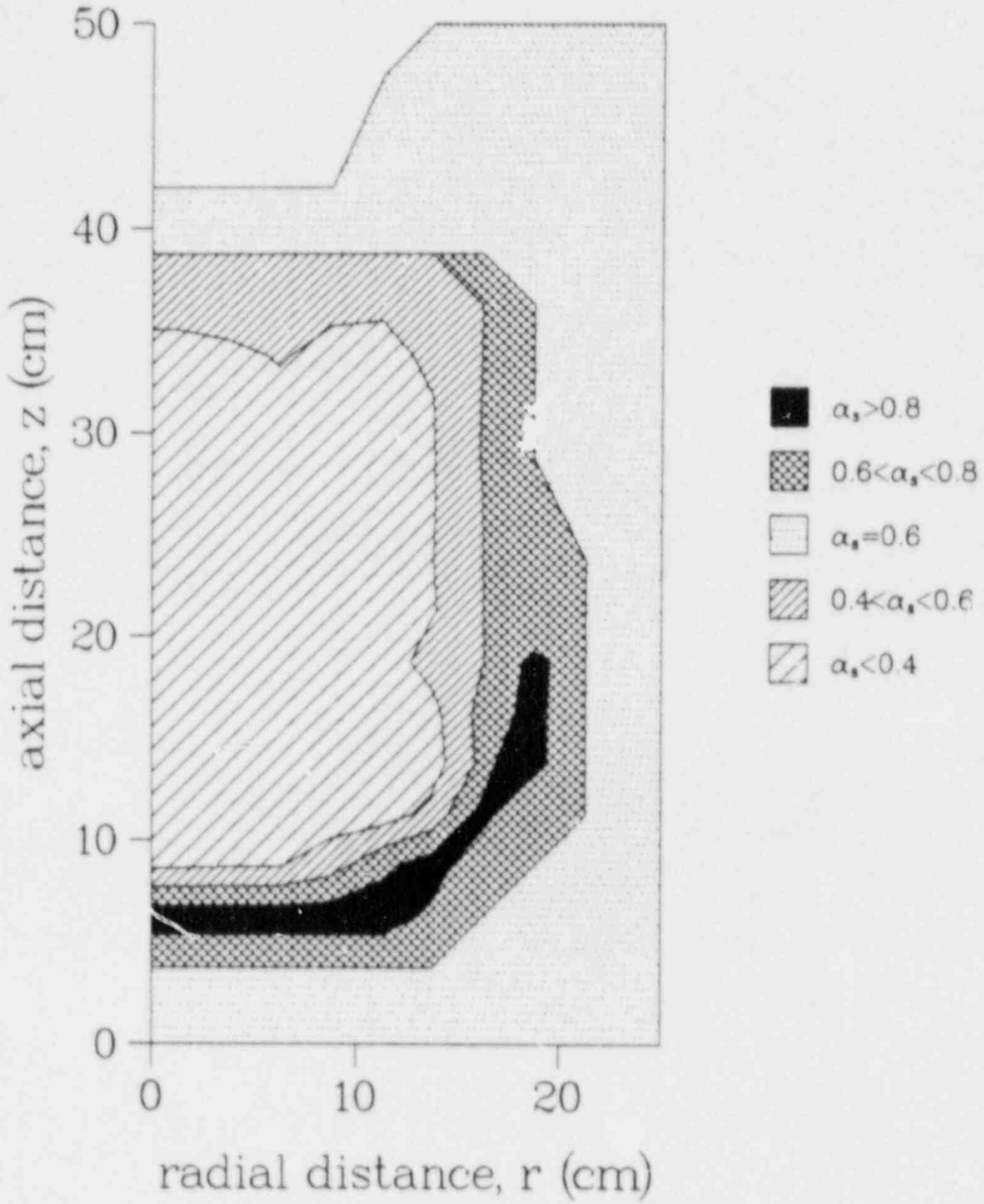

FIG. 37: Solid volume fraction α_s in rubble bed at t=4800 s for a bed with an average particle diameter of 5 mm. The rubble has an initial uniform solid volume fraction of 0.6.

4. CONCLUSIONS

4.1 Summary

A model of melt formation and relocation in a two-dimensional core rubble bed has been developed. The analysis included: mass conservation equations for the species of interest (UO_2 and ZrO_2); a momentum equation (z,r) which represents a balance among drag, capillary and gravity forces; and an energy equation which incorporated the effects of convection by the melt, radiation and conduction through the bed and internal heat generation. An equilibrium UO_2-ZrO_2 phase diagram was prescribed and radiative heat transfer through the bed was incorporated utilizing a temperature dependent conductivity.

A typical solution was presented and the effect of varying the average particle diameter d_p was discussed. Varying d_p had important effects on melting, liquid relocation and crust formation. Increasing d_p resulted in higher effective thermal conductivities, delaying melt formation and decreasing the size of the melt zone. Melt relocation was faster, liquid flowed earlier and refreezing was more vigorous in the bed with large particles.

Materials such as zirconium and stainless steel are currently being incorporated into the present model. Models developed in this study will be implemented in the U.S. Nuclear Regulatory Commission's MELPROG computer code [48,49] and the modified version of the code will be used to analyze the accident at Three Mile Island in considerable detail.

4.2 Major Uncertainties

Experiments are needed both to validate the current core rubble model and to help guide future theoretical work. Major subjects of interest are (1) chemical interactions; (2) flow correlations; and (3) collapsing of high porosity particulate beds. A brief discussion of these issues follows.

Experiments using prototypical materials are needed to test the chemistry models in the analysis. In particular, the use of equilibrium phase diagrams must be assessed. Nonequilibrium behavior can result from both finite reaction rates and finite diffusion rates - the species of interest (UO_2,ZrO_2) are initially separated in core rubble beds. If the equilibrium assumption is adequate, a U-Zr-O phase diagram that represents a minimization of the Gibb's free energy is essential. Especially important is the accurate determination of heats of fusion and dissolution energies for the compounds of interest. Such information will affect predictions of current models. For instance, a recent study indicates that the dissolution of UO_2 by molten Zr is an exothermic process [73], with a heat release on the order of twice the heat of fusion of Zr. Because the current version of the DEBRIS module of MELPROG assumes no heat of dissolution for this reaction, it underpredicts the amount of UO_2 dissolved. Numerical information regarding interactions of U and Zr with Fe, stainless steel, etc., will also be needed.

Melt relocation models in the analysis also need to be validated. Because melt relocation and crust formation is sensitive to flow correlations such as relative permeabilities, the residual saturation and the Leverett function, uncertainties in these correlations can lead to uncertainties in the timing of core slump. To date, none of these correlations have been tested in porous materials undergoing phase changes.

Another important subject of interest is bed collapse. As solid melts and flows downward, the solid density in the center of the bed decreases. Of interest here is the collapse of such high porosity particulate beds. Past experiments indicate that such beds can be self-supporting at fairly low densities. Two explanations have been proposed: (1) liquid trapped between particles by surface tension effects keep the particles in place as they melt; and (2) solid particles sinter as the bed temperature increases (mass diffusion rates increase rapidly with T). Experiments are needed to determine if bed collapse can be represented using a critical porosity. If such a model is adequate, this critical porosity must be determined as a function of particle diameter.

REFERENCES

1. J.E. Kelly, R.J. Henniger and J.F. Dearing, *MELPROG-PWR/MOD1 Analysis of a TMLB' Accident Sequence*, NUREG/CR-4742, SAND86-217, Sandia National Laboratories, Albuquerque, NM (1987).

2. D.R. Olander, "Oxidation of Liquid Zircaloy by Steam," *Journal of Nuclear Materials 119*, pp. 245-250 (1983).

3. D.L. Hagrman, G.A. Reymann and R.E. Mason, *MATPRO-Version 11 (Revision 2): A Handbook of Material Properties for Use in the Analysis of Light Water Reactor Fuel Rod Behavior*, NUREG/CR-0479, Idaho National Engineering Laboratory, Idaho Falls, ID (1981).

4. E.L. Tolman, J.P. Adams, J.L. Anderson, P. Kuan, R.K. McCardell and J.M. Broughton, *TMI-2 Accident Scenario Update*, EGG-TMI-7489, Idaho National Engineering Laboratory, Idaho Falls, ID (1986).

5. D.W. Golden, J.L. Anderson, R.W. Brower, L.J. Fackrell, B.M. Galusha, M.L. Harris, H.E. Knauts, R.D. McCormick, Y. Nomura, C.L. Olaveson, and A. Takizawa, *TMI-2 Standard Problem Package*, EGG-TMI-7382, Idaho National Engineering Laboratory, Idaho Falls, ID (1986).

6. B.A. Cook and E.R. Carlson, "TMI-2 Core Debris Analysis," CONF-8510166, *Proceedings of the First International Information Meeting on the TMI-2 Accident*, Germantown, MD (1985).

7. H. Kouts, *Review of Research on Uncertainties in Estimates of Source Terms from Severe Accidents in Nuclear Power Plants*, NUREG/CR-4883, BNL-NUREG-52061, Brookhaven National Laboratory, Upton, New York (April 1987).

8. M.M. El-Wakil, *Nuclear Heat Transport* (New York, New York: International Textbook Company, 1971) pp. 94-98.

9. R.J. Lipinski, "A Particle-Bed Dryout Model with Upward and Downward Boiling," *Trans. Am. Nuc. Soc. 35*, pp. 358-360 (1980).

10. D. Squarer, L.E. Hochreiter and A.T. Pieczynski, "Modes of Heat Removal From a Heat-Generating Debris Bed," *Nuclear Technology 65*, pp. 16-22 (1984).

11. R.J. Lipinski, "A Review of Debris Coolability Models," *Proceedings of the International Meeting on Light Water Reactor Severe Accident Evaluation*, Cambridge, MA (1983).

12. R.J. Lipinski, "A Coolability Model For Postaccident Nuclear Reactor Debris," *Nuclear Technology 65*, pp. 53-66 (1984).

13. E. Gorham-Begeron, "A One Dimensional Time-Dependent Debris Bed Model," *ASME/JSME Thermal Engineering Joint Conference*, Honolulu, Hawaii (1983).

14. B.D. Turland and K.A. Moore, "One Dimensional Models of Boiling and Dryout," *Proc. 5th Post Accident Heat Removal Information Exchange Mtg.*, Karlsruhe, FRG (1982).

15. B.D. Turland and K.A. Moore, "Debris Bed Heat Transfer with Top and Bottom Cooling," *21st ASME/AIChE Heat Transfer Conference*, Seattle WA (1983).

16. J.B. Rivard, *Post-Accident Heat Removal: Debris Bed Experiments D-2 and D-3*, NUREG/CR-0421, SAND78-1238, Sandia National Laboratories, Albuquerque, NM (1978).

17. J.M. Gronager, M. Schwarz and R.J. Lipinski, *PAHR Debris Bed Experiment D-4*, NUREG/CR-1809, SAND80-2146, Sandia National Laboratories, Albuquerque, NM (1981).

18. G.W. Mitchell, R.J. Lipinski and M. Schwarz, *Heat Removal from a Stratified UO_2-Sodium Particle Bed*, NUREG/CR-2412, SAND81-1622, Sandia National Laboratories, Albuquerque, NM (1982).

19. G.W. Mitchell, C.A. Ottinger and R.J. Lipinski, *The D7 Debris Bed Experiment*, NUREG/CR-3198, SAND82-0062, Sandia National Laboratories, Albuquerque, NM (1983).

20. C.A. Ottinger, G.W. Mitchell, R.J. Lipinski and J.E. Kelly, *The D9 Experiment: Heat Removal from Stratified UO_2 Debris in Sodium*, NUREG/CR-2951, SAND84-1838, Sandia National Laboratories, Albuquerque, NM (1984).

21. G.W. Mitchell, C.A. Ottinger and H. Meister, *The D10 Experiment: Coolability of UO_2 Debris in Sodium With Downward Heat Removal*, NUREG/CR-4055, SAND84-1144, Sandia National Laboratories, Albuquerque, NM (1984).

22. C.A. Ottinger, G.W. Mitchell, A.W. Reed and H. Meister, *Coolability of Stratified UO_2 Debris in Sodium With Downward Heat Removal: The D13 Experiment*, NUREG/CR-4719, SAND86-1043, Sandia National Laboratories, Albuquerque, NM (1987).

23. A.W. Reed, K.R. Boldt, E.D. Gorham-Bergeron, R.J. Lipinski and T.R. Schmidt, *DCC-1/DCC-2 Degraded Core Coolability Analysis*, NUREG/CR-4390, SAND85-1967, Sandia National Laboratories, Albuquerque, NM (1985).

24. K.R. Boldt, A.W. Reed and T.R. Schmidt, *DCC-3 Degraded Core Coolability: Experiment and Analysis*, NUREG/CR-4606, SAND86-1033, Sandia National Laboratories, Albuquerque, NM (1986).

25. V.K. Dhir and I. Catton, *Study of Dryout Heat Fluxes in a Bed of Inductively Heated Particles*, NUREG-0262, University of California at Los Angeles (1977).

26. D. Squarer and J.A. Peoples, "Dryout in Inductively Heated Beds With and Without Forced Flow," *Trans. Am. Nucl. Soc. 34*, p. 535 (1980).

27. H.C. Hardee and R.H. Nilson, "Natural Convection in Porous Media," *Nuclear Science and Engineering 63*, pp. 119-132 (1977).

28. D.H. Cho, D.R. Armstrong II and S.H. Chan, "On the Pattern of Water Penetration into a Hot Particle Bed," *Nuclear Technology 65*, pp. 23-31 (1984).

29. T. Ginsberg, J. Klein, J. Klages and C.E. Schwarz, "Transient Core Debris Bed Heat Removal Experiments and Analysis," *International Meeting on Thermal Nuclear Reactor Safety*, Chicago, Ill. (1982).

30. D.H. Cho, D.R. Armstrong, L.Bova and S.H. Chan, "Debris Bed Quenching Studies," *International Meeting on Thermal Nuclear Reactor Safety*, Chicago, Ill. (1982).

31. N.K. Tutu, T.Ginsberg, J. Klein, J. Klages and C.E. Schwarz, *Debris Bed Quenching Under Bottom Flood Conditions (In-Vessel Degraded Core Cooling Phenomenology)*, NUREG/CR-3850, BNL-NUREG-51788, Brookhaven National Laboratory, Upton, N.Y. (1984).

32. T.Ginsberg, J. Klein, J. Klages, C.E. Schwarz and J.C. Chen, *LWR Steam Spike Phenomenology: Debris Bed Quenching Experiments*, NUREG/CR-2857, BNL-NUREG-51571, Brookhaven National Laboratory, Upton, N.Y. (1982).

33. H.G. Plein and G.A. Carlson, "Debris Bed and Sacrificial Materials Interactions at High Temperatures," *Trans. Am. Nucl. Soc. 30*, p. 436 (1978).

34. H.G. Plein, R.J. Lipinski, G.A. Carlson and D.W. Varela, "Summary of the First Three In-Core PAHR Molten Fuel Pool Experiments," *Proc. Int. Mtg. Fast Reactor Safety Technology I*, Seattle, WA (1979).

35. D.W. Varela, "High-Temperature Magnesium Oxide Interactions with UO_2," *Trans. Am. Nucl. Soc. 34*, p. 546 (1980).

36. D.W. Varela, "Molten Steel Behavior in PAHR Debris Beds," *Trans. Am. Nucl. Soc. 38*, p. 388 (1981).

37. J.T. Hitchcock and J.E. Kelly, "Post-Test Examinations of the In-Pile Molten Pool Experiments," *Trans. Am. Nucl. Soc. 43*, p. 515 (1982).

38. J.T. Hitchcock and J.E. Kelly, *The DC-1 and DC-2 Debris Coolability and Melt Dynamics Experiments*, NUREG/CR-4060, SAND84-1367, Sandia National Laboratories, Albuquerque, NM (1985).

39. C.P. Fryer and J.T. Hitchcock, *The Postirradiation Examination of the DC Melt Dynamics Experiments*, NUREG-CR-4625, SAND86-1102, Sandia National Laboratories, Albuquerque, NM (1987).

40. A.A. Emara and F.A. Kulacki, "A Numerical Investigation of Thermal Convection in a Heat-Generating Fluid Layer," *J. Heat Transfer 102*, pp. 531-537 (1980).

41. A.J. Suo-Anttila and I. Catton, "The Effect of a Stabilizing Temperature Gradient on Heat Transfer From a Molten Fuel Layer with Volumetric Heating," *J. Heat Transfer 102*, pp. 544-548 (1974).

42. F.B. Cheung, "Heat Source-Driven Thermal Convection at Arbitrary Prandtl Number," *J. Fluid Mech. 97*, pp. 743-758 (1980).

43. M. Tveitereid, "Thermal Convection in a Horizontal Fluid Layer with Internal Heat Sources," *Int. J. Heat Mass Trasfer 21*, pp. 335-339 (1977).

44. F.A. Kulacki and R.J. Goldstein, "Thermal Convection in a Horizontal Fluid Layer with Uniform Volumetric Energy Source," *J. Fluid Mech. 55*, pp. 271-287 (1972).

45. L. Baker, R.E. Faw and F.A. Kulacki, "Postaccident Heat Removal-Part I: Heat Transfer Within an Internally Heated, Nonboiling Liquid Layer," *Nuclear Science and Engineering 61*, pp. 222-230 (1976).

46. R.E. Faw and L. Baker, "Postaccident Heat Removal-Part II: Heat Transfer from an Internally Heated Liquid to a Melting Solid," *Nuclear Science and Engineering 61*, pp. 231-238 (1976).

47. J. Morgan, *A New Heat Transfer Model for Density Stratified Molten Pools with Internal Heat Sources*, CLM-R263, Culham Laboratory, Abingdon, Oxfordshire (1986).

48. W.J. Camp et al., *MELPROG-PWR/MOD0: A Mechanistic Code for Analysis of Reactor Core Melt Progression and Vessel Attack under Severe Accident Conditions*, NUREG/CR-4909, SAND85-0237, Sandia National Laboratories, Albuquerque, NM (1987).

49. M.F. Young, J.L. Tomkins and W.J. Camp, "MELPROG Code Development and Methods," *Proceedings of the International Meeting on LWR Severe Accident Evaluation 1*, p.2.8-1, Cambridge, MA (1983).

50. S.S. Dosanjh, *On the Melting and Refreezing of Porous Media*, NUREG/CR-5028, SAND87-1976, Sandia National Laboratories, Albuquerque, NM (1987).

51. A.E. Scheidegger, *The Physics of Flow Through Porous Media*, Third Edition (Toronto and Buffalo: University of Toronto Press, 1974) pp. 266-290.

52. J. Bear, *Dynamics of Fluids in Porous Media* (New York, New York: American Elsevier Publishing Company, Inc., 1972) pp. 439-575.

53. F.A.L. Dullien, *Porous Media Fluid Transport and Pore Structure* (New York, New York: Academic Press, 1979) pp. 251-324.

54. R.A. Greenkorn, *Flow Phenomena in Porous Media* (New York, New York: Marcel Dekker, Inc., 1983) pp. 112-144,497-530.

55. M.C. Leverett, "Capillary Behavior in Porous Solids," *Pet. Trans. AIME 142*, pp.152-169 (1941).

56. C.A. Wert and R.M. Thomson, *Physics of Solids*, Second Edition (New York, New York: McGraw-Hill Book Co., 1970) pp. 71-72.

57. R.B. Bird, W.E. Stewart and E.N. Lightfoot, *Transport Phenomena* (New York, New York: John Wiley and Sons, Inc., 1960) p. 199.

58. G. Hofmann and L. Barleon, "Reduced Coolability of Particle Beds as a Result of Capillary Effects at Horizontal Phase Boundaries," *Proceedings of the International ANS/ENS Topical Meeting on Thermal Reactor Safety*, San Diego, California, February 2-6, 1986.

59. G.G. Brown and Associates, *Unit Operations*, Sixth Edition (New York, New York: John Wiley and Sons, Inc., 1956) pp. 210-228.

60. J.E. Kelly, J.T. Hitchcock and M.L. Schwarz, "Heat Transfer Characteristics of Dry Porous Particulate Beds with Internal Heat Generation," *ASME-JSME Thermal Engineering Joint Conference Proceedings*, Honolulu, Hawaii (March 1983).

61. A.V. Luikov, A.G. Shashkov, L.L. Vasiliev and Yu.E. Fraiman, "Thermal Conductivity of Porous Systems," *Int. J. Heat Mass Transfer 11*, p. 117 (1968).

62. D. Vortmeyer, "Radiation in Packed Solids," Sixth Int. Heat Trans. Conf., Toronto (1978).

63. W. Schote, "Thermal Conductivity of Packed Beds," *A.I.Ch.E. Journal 6*, p.63 (1960).

64. S. Imura and E. Takegoshi, "Effect of Gas Pressure on the Effective Thermal Conductivity of Packed Beds," *Heat Transfer Japanese Research 3*, p.13 (1974).

65. D.L. Hagrman, *Materials Properties Models for Zirconium-Uranium Oxygen Melting, (PSOL,PLIQ), Solution, and Precipitation (ZUSOLV)*, Idaho National Engineering Laboratory, Idaho Falls, ID (1985).

66. D.L. Hagrman, *Material Property Models for Severe Core Damage Analysis*, EGG-CDD-5801, Idaho National Laboratory, Idaho Falls, ID (1982).

67. C.S. Kim, A. Blomquist, J. Haley, R. Land, J. Fischer, M.G. Chasanov and L. Leibowitz, "Measurement of the Thermal Diffusivity of Molten UO_2," *Proceedings of the Seventh Symposium on Thermophysical Properties*, Gaithersburg, MD (1977).

68. H.A. Tasman, D. Pel, J. Richter and H.E. Schmidt, "Measurement of the Thermal Conductivity of Liquid Uranium Dioxide," *Proceedings of the Eighth European Thermophysical Properties Conference*, Baden-Baden, pp. 301-313 (1982).

69. J.K. Fink, M.G. Chasanov and L. Leibowitz *Thermodynamic Properties of Uranium Dioxide*, ANL-CEN-RSD-80-3, Argonne National Laboratory, Illinois (1981).

70. J.K. Fink, M.G. Chasanov and L. Leibowitz, *Transport Properties of Uranium Dioxide*, ANL-CEN-RSD-80-4, Argonne National Laboratory, Illinois (1981).

71. J.K. Fink and L. Leibowitz, *An Analysis of Measurements of the Thermal Conductivity of Liquid Urania*, ANL-CEN-RSD-83-1, Argonne National Laboratory, Illinois (1983).

72. J.K. Fink, M.G. Chasanov and L. Leibowitz, *Properties for Reactor Safety Analysis*, ANL-CEN-RSD-82-2, Argonne National Laboratory, Illinois (1982).

73. J.L. Brimhall and J.T. Prater, *Heat of Reaction of Molten Zirconium with UO_2*, NUREG/CR-4890, PNL-6165, Pacific Northwest Laboratory, Richland, WA (1987).

U.S. Government Printing Office
Receiving Branch (Attn: NRC Stock)
8610 Cherry Lane
Laurel, MD 20707
250 copies for R7

U.S. Nuclear Regulatory Commission (23)
Office of Nuclear Regulatory Research
Division of Reactor System Safety
Washington, DC 20555
Attn: D. Ross
M. Silberberg
G. Marino
C. Kelber
J. Mitchell
R. Meyer
L. Chan
J. Han (5)
P. Worthington
R. Wright (5)
R. VanHouten
B. Burson
T. Walker
P. Wood
T. Lee

U.S. Nuclear Regulatory Commission
Office of Nuclear Reactor Regulation
Washington, DC 20555
Attn: R. Palla

U.S. Department of Energy
Office of Nuclear Safety Coordination
Washington, DC 20545
Attn: R. W. Barber

U.S. Department of Energy (2)
Albuquerque Operations Office
P. O. Box 5400
Albuquerque, NM 87185
Attn: J. R. Roeder, Director
Transportation Safeguards Division
J. A. Morley, Director
Energy Research Technology Division

Argonne National Laboratory
9700 South Cass Avenue
Argonne, IL 60439
Attn: W. Sha

Battelle Columbus Laboratory (2)
505 King Avenue
Columbus, OH 43201
Attn: R. Denning
P. Cybulskis

Battelle Northwest (2)
P. O. Box 999
Richland, WA 99352
Attn: F. Panisko
D. Lanning

Brookhaven National Laboratory (3)
Upton, NY 11973
Attn: R. A. Bari
T. Ginsberg
M. Khatib-Rhabar

Electric Power Research Institute
P. O. Box 10412
Palo Alto, CA 94303
Attn: R. Sehgal (2)

Los Alamos National Laboratory (8)
P. O. Box 1663
Los Alamos, NM 87545
Attn: J. Dearing (5)
E. Fugelso
D. Liles
M. Sahota

Oak Ridge National Laboratory (2)
P. O. Box Y
Oak Ridge, TN 37830
Attn: T. Kress
S. Hodge

EG&G Idaho (4)
P. O. Box 1625
Idaho Falls, ID 83415
Attn: C. Allison
P. Bayless
J. Dahlman
P. Wheatley

University of Wisconsin
Nuclear Engineering Department
1500 Johnson Drive
Madison, WI 53706
Attn: M. L. Corradini

H. Bairiot
Belgonucleaire S. A.
Rue de Champ de Mars 25
B-1050 Brussels
BELGIUM

D. Haas
Belgonucleaire S. A.
Rue de Champ de Mars 25
B-1050 Brussels
BELGIUM

P. Fehrenbach
Atomic Energy Canada Ltd.
Chalk River, Ontario
CANADA K0J 1J0

M. Notley
Atomic Energy Canada Ltd.
Chalk River, Ontario
CANADA K0J 1J0

D. Nishimura
Atomic Energy Canada Ltd.
Chalk River, Ontario
CANADA K0J 1J0

H. Rosinger
Atomic Energy Canada Ltd.
Pinawa, Manitoba
CANADA ROE 1LO

J. P. Longworth
Central Electric Generating Board
Berkeley Nuclear Labs
Berkeley, Gloucester GL13 9PB
ENGLAND

M. Hayns
UK Atomic Energy Authority
SRD
Culcheth, Warrington WA3 4VE
ENGLAND

UK Atomic Energy Authority (3)
RX Systems Analysis Div.
Winfrith, Dorchester
Dorset DT2 8DH
ENGLAND
Attn: R. Potter
S. Kinnersley
J. Lillington

B. Turland
UK Atomic Energy Authority
Culham Laboratory
Oxon 0X14 30B
Abingdon
ENGLAND

J. Stephenson
UK Atomic Energy Authority
SRD
Culcheth, Warrington WA3 4VE
ENGLAND

A. Fiege
Kernforschungszentrum
Postfach 3640
7500 Karlsruhe
FEDERAL REPUBLIC OF GERMANY

S. Hagen
Kernforschungszentrum
Postfach 3640
7500 Karlsruhe
FEDERAL REPUBLIC OF GERMANY

P. Hoffman
Kernforschungszentrum
Postfach 3640
7500 Karlsruhe
FEDERAL REPUBLIC OF GERMANY

M. Rininsland
Kernforschungszentrum
Postfach 3640
7500 Karlsruhe
FEDERAL REPUBLIC OF GERMANY

G. Petrangeli, Dire R. D. S.
Enea Nucl Energ Alt Disp
Via V Brancati 48
00144 Rome
ITALY

G. Saponaro
Enea Nucl Energ Alt Disp
Via Regina Marg-125
00144 Rome
ITALY

K. Hirano
Japan Atomic Energy Res. Inst.
Tokai-Mura Naka-Gun
Ibaraki-Ken 319-11
JAPAN

S. Saito
Japan Atomic Energy Res. Inst.
Tokai-Mura Naka-Gun
Ibaraki-Ken 319-11
JAPAN

K. Soda
Japan Atomic Energy Res. Inst.
Tokai-Mura Naka-Gun
Ibaraki-Ken 319-11
JAPAN

J. H. Cha
Korea Adv. Energy Research Inst.
P. O. Box 7
Cheung-Ryang
Seoul
SOUTH KOREA

S. K. Chae
Korea Adv. Energy Research Inst.
P. O. Box 7
Daeduk Danji
Choong m
SOUTH KOREA

H. R. Jun
Korea Adv. Energy Research Inst.
P. O. Box 7
Daeduk Danji
Chungnam
SOUTH KOREA

K. J. Brinkmann
Netherlands Energy Res. Fdtn.
P. O. Box 1
1755ZG Petten NH
NETHERLANDS

Chao-Chin Tung
Atomic Energy Council
67 Lane 144 Sec 4
Keelung Rd.
Taipei, Taiwan
REPUBLIC OF CHINA

Sen-I Chang
Institute of Nuclear Energy Res.
P. O. Box 3
Lungtan
Taiwan 325
REPUBLIC OF CHINA

K. Johansson
Studsvik Energiteknik AB
S-611 82 Nykoping
SWEDEN

J. Bagues
Consejo de Seguridad Nuclear
Sor Angela de la Cruz 3
Madrid 28046
SPAIN

C. Graeslund
Statens Karnkraftinspektion
P. O. Box 27106
S-10252 Stockholm
SWEDEN

Sandia Distribution:
3141 S. A. Landenberger (5)
3151 W. L. Garner
6400 D. J. McCloskey
6415 F. E. Haskin
6418 J. E. Kelly
6420 J. V. Walker
6422 D. A. Powers
6422 W. W. Tarbell
6423 K. O. Reil
6423 R. O. Gauntt
6423 B. W. Marshall, Jr.
6425 W. J. Camp
6425 S. S. Dosanjh (22)
6425 R. D. Gasser
6425 T. J. Heames
6425 A. W. Reed
6425 R. C. Schmidt
6425 R. C. Smith
6425 J. L. Tomkins
6425 C. J. Wheatley
6425 K. A. Williams
6425 M. F. Young
6427 M. Berman
6429 K. D. Bergeron
8524 P. W. Dean

NRC FORM 335 (2.84) NRCM 1102, 3201, 3202

U.S. NUCLEAR REGULATORY COMMISSION

BIBLIOGRAPHIC DATA SHEET

SEE INSTRUCTIONS ON THE REVERSE

1 REPORT NUMBER (Assigned by TIDC add Vol. No., if any)

NUREG/CR-5029
SAND87-2303

2 TITLE AND SUBTITLE

MELT PROGRESSION IN SEVERELY DAMAGED REACTOR CORES

3 LEAVE BLANK

4 DATE REPORT COMPLETED

MONTH	YEAR
September	1987

5 AUTHOR(S)

6 DATE REPORT ISSUED

MONTH	YEAR
December	1987

7 PERFORMING ORGANIZATION NAME AND MAILING ADDRESS (Include Zip Code)

Reactor Safety Theoretical Physics Division
Sandia National Laboratories
P. O. Box 5800
Albuquerque, NM 87185

8 PROJECT/TASK/WORK UNIT NUMBER

9 FIN OR GRANT NUMBER

A1042

10 SPONSORING ORGANIZATION NAME AND MAILING ADDRESS (Include Zip Code)

Fuel Systems Research Branch
U.S. Nuclear Regulatory Commission
Washington, DC 20555

11a TYPE OF REPORT

Final Report

b PERIOD COVERED (Inclusive dates)

12 SUPPLEMENTARY NOTES

13 ABSTRACT (200 words or less)

A model of melt formation and relocation in a two-dimensional core rubble bed is developed in this report. The analysis includes mass conservation equations for the species of interest (UO_2 and ZrO_2); a liquid momentum equation (z,r,) that incorporates the effects of drag, gravity and capillary forces; and an energy equation that includes internal heat generation by decay heating, convection by the liquid and the solid (as it collapses) as well as conduction and radiation through the bed. An equilibrium UO_2-ZrO_2 phase diagram is prescribed and radiative heat transfer through the bed is incorporated utilizing a temperature-dependent thermal conductivity.

Models developed in this work will be implemented in the MELPROG computer code that is being developed by Sandia and Los Alamos National Laboratories. The modified version of MELPROG will then be used to calculate melt progression, crust growth, pool formation, crust failure and the relocation of debris material into the lower plenum during the Three Mile Island accident and other nuclear reactor accidents.

14 DOCUMENT ANALYSIS - a KEYWORDS/DESCRIPTORS

Core debris, core meltdown, reactor safety

b IDENTIFIERS/OPEN-ENDED TERMS

15 AVAILABILITY STATEMENT

Unlimited

16 SECURITY CLASSIFICATION

(This page) Unclassified

(This report) Unclassified

17 NUMBER OF PAGES

70

18 PRICE

8804080274

☆ U.S. GOVERNMENT PRINTING OFFICE: 1988—773-049/61033